



Two-dimensional transition metal dichalcogenides beyond MoS₂ for the catalytic reduction of nitroarenes: MoSe₂ exhibits enhanced performance

A. Martínez-Jódar^{a,*}, S. Villar-Rodil^{a,*}, M.A. Salvadó^{b,*}, D.F. Carrasco^a, P. Pertierra^b, J.M. Recio^b, J.I. Paredes^{a,*}

^a Instituto de Ciencia y Tecnología del Carbono, INCAR-CSIC, C/Francisco Pintado Fe 26, 33011 Oviedo, Spain

^b MALTA-Consolider Team and Departamento de Química Física y Analítica, Universidad de Oviedo, 33006 Oviedo, Spain

ARTICLE INFO

Keywords:

Transition metal dichalcogenides (TMDs)

Nanocatalysts

MoSe₂

MoS₂

Nitroarene reduction

ABSTRACT

Two-dimensional (2D) MoSe₂ nanosheets were investigated as a catalyst for nitroarene reduction in the context of water treatment and demonstrated to exhibit a higher activity than their more studied MoS₂ counterpart. Density functional theory (DFT) calculations disclosed a feasible nitroarene reduction pathway on 2D MoSe₂, which involved passivation of the active site by oxygen from the nitro group and its reactivation by a reducing hydride. DFT analysis also provided an explanation for the isomer selectivity displayed by the 2D MoSe₂ catalyst (towards, e.g., 2-, 3- and 4-nitroaniline). To facilitate their practical implementation, the bare MoSe₂ nanosheets were coated with colloidal stabilizers, and were also immobilized on polymer foam, where they could be re-used for several consecutive catalytic cycles with no significant loss of activity. Overall, the present results open the prospect of 2D transition metal dichalcogenides beyond MoS₂ as competitive nanocatalysts for the reduction of nitroarenes and other organic compounds.

1. Introduction

Over the last decade, two-dimensional (2D) materials have been extensively investigated for their prospective use in the field of (thermo/electro/photo)catalysis, whether as catalysts themselves or in a supporting role to the catalyst proper [1–5]. Specific 2D materials of interest in this realm include graphene, phosphorene as well as other mono-elemental systems, transition metal dichalcogenides (TMDs), MXenes and graphitic carbon nitride, among others [1,2]. Apart from the particular benefits that certain chemical compositions and crystal structures may bring, the attraction of 2D solids in catalysis stems from some general features of theirs, which comprise the following: (1) The large surface area (high surface-to-volume ratio) associated to their nanometric or atomic thickness implies that catalytic active sites readily accessible to the reacting substrates can be present in very high numbers, and also that 2D materials can host large numbers of nanoparticles, atomic clusters or single atoms when the former are used as a catalyst support for the latter [5,6]. (2) The electron confinement effect derived from the 2D morphology leads to changes in electronic states that can potentially alter the chemical reactivity of the active sites in the material compared to its bulk counterpart and other nanostructured

forms, and thus the course and/or rate of catalytic reactions [1,6]. (3) The high mechanical flexibility of 2D solids that is derived from their large aspect ratio implies that they are very efficient at conformally coating other materials (e.g., catalytic particles). As a result, they can afford strongly confined reaction environments, where the course and/or rate of chemical reactions can be changed relative to the unconfined case (“catalysis under cover”) [7]. In other cases, the conformal 2D coating provides a protective layer for catalysts that are unstable under harsh reaction conditions, such as those based on non-precious metals, so that the reaction is steered by the underlying catalyst but actually takes place on the surface of the 2D material (“chainmail for catalyst”) [8].

Within the broad family of 2D materials for catalysis, TMDs and, in particular, 2D MoS₂ are currently the focus of especial interest owing to their high activity as electrocatalysts for a number of all-important chemical processes [9,10]. These electrocatalytic processes encompass the hydrogen evolution reaction (HER) first and foremost, but also the oxygen reduction reaction or the CO₂ and N₂ reduction reactions [9,11,12]. Nonetheless, 2D TMD-based catalysts have also shown in recent years their promise in other relevant applications. This is specifically the case of the reduction of nitroarenes [13], which is of practical interest in

* Corresponding authors.

E-mail addresses: silvia@incar.csic.es (S. Villar-Rodil), mass@uniovi.es (M.A. Salvadó), paredes@incar.csic.es (J.I. Paredes).

<https://doi.org/10.1016/j.apcatb.2023.123174>

Received 4 May 2023; Received in revised form 1 August 2023; Accepted 11 August 2023

Available online 14 August 2023

0926-3373/© 2023 The Author(s). Published by Elsevier B.V. This is an open access article under the CC BY-NC-ND license (<http://creativecommons.org/licenses/by-nc-nd/4.0/>).

the synthesis of fine chemicals as well as in the area of water treatment for environmental remediation. For instance, the production of some widely used pharmaceutical drugs (e.g., paracetamol), agrochemical compounds and dyes relies on the availability of certain substituted anilines as key intermediates, which can be accessed via reduction of their corresponding nitroarenes [14,15]. Likewise, many substituted nitroarenes (e.g., nitrophenols) are frequently found in industrial effluents, but the toxic and recalcitrant nature of such compounds advises against their direct release to natural water bodies. In this context, degradation of the nitroarenes by way of their reduction prior to disposal is one workable option, since the reduced products (i.e., anilines) are much more biodegradable and less hazardous than their nitroarene counterparts [16,17].

Similar to the case of the above electrocatalytic reactions, the allure of 2D TMDs as catalysts for nitroarene reduction arises from the fact that they are more affordable and earth-abundant alternatives to the noble metal-based catalysts commonly used for such reactions [14,16,18]. Here again, MoS₂ nanosheets and other nanostructures have been the TMD-based catalysts of choice in most previous studies [13,19–31]. While such a preference is very likely based on the wider availability of MoS₂ relative to other TMDs, it may not be completely justified from the perspective of catalyst performance. However, so far very little work has been carried out on the catalytic activity of other TMDs in any nanostructured form toward nitroarene reduction [32–34], let alone work directly comparing their activity with that of MoS₂. Moreover, the atomic-level understanding of the interactions between these substrate molecules and the active sites of TMD catalysts is currently very limited. Such active sites are thought to be located at coordinatively unsaturated metal centers of edges and chalcogen vacancies on the surface of the TMD lattice [25,29,33], very much like the active sites for the HER and other electrocatalytic reactions [9–12]. Having this type of physical insight would be expected to shed light on experimentally observed differences in the activity of a given TMD catalyst toward, e.g., different substituted nitroarenes. In particular, it would shed light on differences in catalyst activity toward different structural isomers of a given substituted nitroarene, which could be a priori the most difficult to rationalize.

In an effort to contribute to addressing these issues, we have investigated the use of 2D MoSe₂ nanosheets as a catalyst for the reduction of nitroarenes with sodium borohydride (NaBH₄) as the reductant, the results of which are reported here. Even though it is the closest relative of MoS₂ within the family of TMD compounds, MoSe₂ possesses some features that make it potentially a strong competitor of the former and thus worth exploring in the catalytic reduction of nitroarenes, as well as in other catalytic and non-catalytic applications [35,36]: (1) MoSe₂ is a reasonably affordable material. (2) The longer bond length and lower bond energy of MoSe₂ compared with those of MoS₂ render catalytically active structural defects (edges, chalcogen vacancies) easier to form [37] and, therefore, suggest that they could be intrinsically more abundant in the former TMD. (3) Due to the higher metallicity of MoSe₂ (lower electronegativity of selenium compared to sulfur), electronic charges taking part in reduction reactions at the catalytic active sites of this TMD could be more readily available compared to the case of MoS₂. We note that (2) and (3) would imply 2D MoSe₂ nanosheets to be more catalytically active in reduction reactions than their MoS₂ counterpart. In this work, we demonstrate that this is generally the case for the reduction of nitroarenes and provide some insight into the origin of such higher activity. Moreover, with the assistance of density functional theory (DFT)-based calculations, we probe into the unexpected activity trends that were observed for 2D MoSe₂ nanosheets toward nitroarene isomers in our experiments. The results point to differences in the adsorption configuration of the isomers as a main driver of the reported activity trends with the MoSe₂ catalyst. Overall, the present work opens the prospect of 2D TMDs beyond MoS₂ as competitive catalysts for nitroarene reduction for water treatment and suggests some guidelines to pinpoint the most promising candidates as well as to rationalize

catalytic activity trends.

2. Experimental and computational methods

2.1. Materials and reagents

MoS₂ and MoSe₂ powder materials were purchased from Alfa Aesar. The following chemicals were acquired from Sigma-Aldrich: DMF, isopropanol, NaBH₄, hydrazine monohydrate, 4-nitroaniline (4-NA), 3-nitroaniline (3-NA), 2-nitroaniline (2-NA), 4-nitrophenol (4-NP), 3-nitrophenol (3-NP), 2-nitrophenol (2-NP), nitrobenzene (NB), methyl orange (MO), potassium hexacyanoferrate {K₃[Fe(CN)₆]}, adenosine monophosphate (AMP), [(poly(ethylene glycol)-*block*-poly(propylene glycol)-*block*-poly(ethylene glycol)) (P-123). All the materials and chemicals were used as received, without further treatment. Milli-Q deionized water (Millipore Corporation; resistivity: 18.2 MΩ cm) was used throughout the experiments.

2.2. Preparation of exfoliated MoSe₂ and MoS₂ nanosheets in aqueous dispersion

MoS₂ and MoSe₂ nanosheets (NSs) were obtained from the direct exfoliation of the corresponding bulk powders in DMF with the assistance of sonication. Specifically, TMD powder at nominal concentration of 30 g mL⁻¹ in DMF was bath-sonicated (J.P. Selecta Ultrasons system, 40 kHz) for 5 h (changing from bath to bath to avoid overheating of water). The resulting suspension was centrifuged (Eppendorf 5430 microcentrifuge) at 200 g for 20 min to sediment the non- and poorly delaminated fractions of the material and the supernatant containing well-exfoliated flakes was collected. Then the TMD dispersion was diluted in DMF to ~0.2 mg mL⁻¹ and the solvent was exchanged by water by subjecting the colloidal dispersion to four cycles of high-speed centrifugation (21,191 g, 25 min) to completely sediment the exfoliated flakes followed by re-suspension in deionized water by bath-sonication (~2 min). The resulting aqueous TMD suspensions were adjusted to a concentration ~0.10–0.15 mg mL⁻¹, and used in all the subsequent experiments. To determine the concentration of the TMD dispersions, the absorbance of the as-prepared dispersion was measured and a known volume was vacuum-filtered through polycarbonate filters and dried overnight under vacuum, allowed to cool down in a desiccator and finally weighed to calculate its original concentration. The extinction coefficient (ε) values derived from such measurements for MoS₂ and MoSe₂ were ε_{MoS₂} (λ = 345 nm) = 34.5 and ε_{MoSe₂} (λ = 365 nm) = 24.5 mg⁻¹ L cm⁻¹, respectively.

2.3. Generation of selenium vacancies in MoSe₂ nanosheets by hydrazine treatment

To generate selenium vacancies in the exfoliated MoSe₂ flakes, a mixture of MoSe₂ aqueous dispersion with hydrazine monohydrate with a ratio of 1 mL hydrazine per 100 mg of exfoliated MoSe₂ was poured into a test tube, which was then capped with a rubber septum with a small orifice to allow gas release. The mixture was heated at 70 °C for one hour, after which the reacted product was washed to remove any hydrazine monohydrate remaining in the solution by applying three consecutive cycles of sedimentation via centrifugation (21,191 g, 20 min), replacement of all the supernatant volume by neat water and re-dispersion of the MoSe₂ flakes by a brief (~2 min) sonication step.

2.4. Catalytic activity tests of MoSe₂ and MoS₂ nanosheets toward nitroarene reduction

For the catalytic tests, aqueous aliquots (2.5 mL) containing TMD catalyst at concentration of 14 μg mL⁻¹, 0.11–0.12 mM of nitroarene, as well as a large excess of NaBH₄ (112 mM) were prepared in quartz cuvettes with an optical path length of 1 cm, which were immediately

transferred to an UV-Vis absorption spectrophotometer. The reaction progress was monitored by measuring the evolution of absorbance at the wavelength of the maximum of a characteristic peak of the substrate molecule versus time. The extinction coefficients of the different substrate materials at such wavelengths at the conditions of catalysis were determined by calibration in the presence of 112 mM NaBH₄ [ϵ (3-nitrophenolate, λ = 390 nm) = 1456 M⁻¹ cm⁻¹; ϵ (2-nitrophenolate, λ = 416 nm) = 4643 M⁻¹ cm⁻¹; ϵ (4-NA, λ = 380 nm) = 12,502 M⁻¹ cm⁻¹; ϵ (3-NA, λ = 357 nm) = 1418 M⁻¹ cm⁻¹; ϵ (2-NA, λ = 416 nm) = 4390 M⁻¹ cm⁻¹; ϵ (NB, λ = 270 nm) = 7451 M⁻¹ cm⁻¹] or, in the case of 4-NP, taken from the literature [ϵ (4-nitrophenolate; λ = 400 nm) = 17,500 M⁻¹ cm⁻¹ [38]]. For some selected nitroarenes (4-NP, 4-NA and 3-NA), catalytic tests were performed with a higher substrate concentration of 1 mM, as well as an excess of NaBH₄ (224 mM), keeping the catalyst concentration at 14 μ g mL⁻¹. In such cases, the reaction progress was monitored by measuring the evolution of absorbance at a wavelength characteristic of the substrate where saturation of the signal at such higher concentration was avoided (455 nm for 4-NP [26], 445 nm for 4-NA, and 357 nm for 3-NA).

2.5. Characterization techniques

The materials were characterized by UV-Vis absorption spectroscopy, Atomic Force microscopy (AFM), Field-emission scanning transmission microscopy (FE-SEM), Scanning transmission electron microscopy (STEM), High resolution transmission electron microscopy (HR-TEM), energy dispersive X-ray spectroscopy (EDX), selected area diffraction (SAED), Dynamic light scattering (DLS), X-ray photoelectron spectroscopy (XPS), X-ray diffraction (XRD), Raman spectroscopy, Electron paramagnetic resonance (EPR) and measurement of zeta potential. UV-Vis absorption/extinction spectra of TMD dispersions were recorded with a double-beam Genesys 180 spectrophotometer (Thermo Fisher Scientific). AFM imaging was performed in a Nanoscope IIIa Multimode system in the tapping mode of operation and using rectangular silicon cantilevers with resonance frequencies of 250–300 kHz and nominal spring constant of 40 N m⁻¹. To image exfoliated TMD flakes by AFM, the delaminated material was dispersed in water (~0.01 mg mL⁻¹), drop-cast (10–20 μ L) onto a freshly cleaved mica substrate and dried overnight under a vacuum at 60 °C. The recorded AFM images were analyzed with SPIP software (Image Metrology). FE-SEM and STEM imaging were carried out in a Quanta FEG apparatus (FEI Company) working at a bias voltage of 20–25 kV. Specimens for FE-SEM (melamine foam) were mounted onto the sample-holder by means of double-sided carbon adhesive tape, while those for STEM and HR-TEM were prepared by drop-casting a few microliters of the sample dispersion in water and isopropanol, respectively, onto a copper grid (200 square mesh) covered with a thin continuous carbon film (STEM) or lacey carbon (HR-TEM), and allowing it to dry under ambient conditions. HR-TEM, EDX and SAED were carried out with a JEOL JEM-2100 F instrument operated at an accelerating voltage of 200 kV and equipped with Scanning transmission electron microscope (STEM) control unit (Gatan), energy dispersive X-ray (EDX) detector (Oxford Instruments, silicon drift detector (SDD) 80 mm²), CCD camera (14-bit Gatan Orius SC600), and bright-field and high angle annular dark field (HAADF) detectors (JEOL). DLS measurements of the TMD dispersions were performed using a 3DDLS photon cross-correlation spectrometer (LS Instruments), equipped with a He-Ne laser (632.8 nm). The measurements were carried out in quintuplicate at 25 °C and at an angle of 90° for 100 s for each measurement and using the 3D correlation mode. XPS was carried out on a SPECS system equipped with a Phoibos 100 hemispherical electron energy analyzer. The spectra were recorded at a take-off angle of 90°, working at a pressure below 10⁻⁷ Pa and using a monochromatic aluminum X-ray source operated at a voltage of 14.00 kV and a power of 175 W. The photoexcited electrons were analyzed in the constant pass energy mode, using a pass energy of 50 eV for survey spectra and 10 eV for high resolution core-level spectra. CasaXPS

software was used for data processing. Core level curve fitting in different components was performed using a Shirley background and a standard least squares algorithm. Each component was considered as a convolution of a Gaussian and a Lorentzian function (80:20). In the S 2p core level band, each chemical state is represented by a spin-orbit doublet with spin-orbit splitting (SOS) constant of 1.16 eV, as expected for an ideal sulphur signal, and an approximately 1:2 peak area ratio between S 2p_{1/2} and S 2p_{3/2} components, actually, relative sensitivity factor (RSF) (S 2p_{1/2})/RSF (S 2p_{3/2}) = 0.567/1.11 = 0.511 [39]. In the Mo 3d and Se 3d core level bands, each chemical state is a spin-orbit doublet with area ratio between 3d_{3/2} and 3d_{5/2} components of approximately 2:3, actually, RSF (Mo 3d_{3/2})/RSF (Mo 3d_{5/2}) = 3.88/5.62 = 0.69 and RSF (Se 3d_{3/2})/RSF (Se 3d_{5/2}) = 0.934/1.36 = 0.69 [39] with a SOS constant of 3.15 eV and 0.86 eV, for Mo 3d and Se 3d, respectively. XRD diffractograms were acquired on a Bruker D8 Advance diffractometer equipped with a Cu K α anode. The data were recorded in a 2 θ range of 5–80° with a step size of 0.015° and time per step of 6 s for XRD measurements, the starting TMD powders were used as received while the exfoliated materials were prepared in the form of films by filtering from dispersion through polycarbonate membranes with pore size of 50 μ m (Nucleopore™, Whatman®). Raman spectra were acquired with a Renishaw inVia Qontor instrument, working at a laser excitation wavelength of 532 nm (green line). To avoid or minimize damage to the sample, the incident laser power was set to values below 0.5 mW. Samples for XPS and Raman spectroscopy were prepared by drop-casting the aqueous exfoliated TMD dispersions onto metallic sample holders until uniform films covered the substrate and allowing them to dry under ambient conditions. The starting TMD powders were pressed into pellets by means of a hydraulic press. EPR spectra were recorded with a X-Band (9.4 GHz) Bruker ELEXSYS E500 spectrometer using a magnetic field modulation amplitude of 2 G, a modulation frequency of 100 kHz, a time constant of 20.48 s and a microwave power of ~20 mW. The determination of the zeta potential was performed from electrophoretic mobility measurements using in a Zetasizer Nano-Z instrument (Malvern) equipped with a laser light source with a wavelength of 633 nm. The zeta potential was calculated using the Smoluchowski equation.

2.6. Computational methods

Computational calculations were performed under the density functional theory (DFT) framework using the Vienna Ab-initio Software Package (VASP) [40,41]. For the exchange-correlation energy term, the Perdew-Burke-Ernzerhof (PBE) functional was selected [42]. The simulation cell consisted of a 2H-MoSe₂ 4 \times 4 monolayer. Periodic images along the *c* axis were separated by a vacuum slab of 18 Å. Starting from this structure, models with one (1 V_{Se}) and four (4 V_{Se}) selenium atom vacancies (on the same side of the layer) per supercell were built. For the adsorbed states, one nitroarene molecule per supercell was placed over one of the selenium vacancies. All the models were optimized (coordinates and the cell parameters *a* and *b*) with the *c* axis length fixed at 18 Å. Optimizations were stopped when the forces and stresses were less than 0.01 eV Å⁻¹. An energy cutoff of 450 eV was used for the plane wave basis set. Due to the large size of the supercells used here, only the Γ point was sampled in the reciprocal space. Nitroarene molecules in the absence of surface were optimized using fixed cells of 18 \times 18 \times 18 Å³. In those reaction intermediates where the molecule was expected to be negatively charged, one sodium atom was included to maintain the electrical neutrality of the system. Structural models were built using PowderCell [43] and VESTA [44]. Structure plots were made with VESTA.

2.7. Identification of reaction intermediates

Some reaction intermediates for 3-NA reduction were identified by means of reversed-phase (RP) ultrahigh-performance liquid

chromatography (UHPLC) (UltiMate™ Dionex 3000 HPLC system from Thermo Scientific) coupled to high-resolution mass spectrometry (HR-MS) (IMPACT II ESI-QTOF instrument from Bruker). 3-NA and its reaction product, 1,3-phenylenediamine, were also detected. The catalysis medium was prepared (2.5 mL) and the reaction was arrested after certain reaction times by removing the catalyst by syringe-filtration (Whatman® Anotop® syringe filter 0.02 μm alumina-based membrane) directly into solid phase extraction (SPE) cartridges (HLB Oasis 250cc, Waters), previously conditioned in ultrapure water (reagent grade type I, Autowomatic, Wasserlab). After sample introduction and a cleaning step with water, analytes were eluted with absolute methanol (6 mL, LC-MS grade, OPTIMA, Thermo Fisher), and collected in a glass vial. Off-line SPE eliminated NaBH_4 , whose presence would have been detrimental to the ionization of the analytes needed for HR-MS detection. 300 μL was immediately transferred into liquid chromatography vials (300 μL insert vials, Thermo Scientific). Luna Omega Polar column (150 \times 2.1 mm, 1.7 μm , Phenomex) column was used as stationary phase while the mobile phase was a mixture of: (A) ultrapure water, and (B) acetonitrile (LC-MS grade, OPTIMA, Thermo Fisher), both with 0.1%

v/v formic acid (LC-MS grade, Thermo Fisher). 5 μL was injected and separated applying the following program: 0 min 30% B, 2 min 30% B, 10 min 55% B, 11 min 70% B, 13 min 70% B. HR-MS detection was performed in full-scan (50–1500 M/Z) positive mode. CompassDataAnalysis software (V4.4, Bruker) was used for spectra analysis. A combination of exact mass and isotopic pattern was taken into consideration for molecular formula proposal of potential catalysis intermediates. In all cases, $\text{M}+\text{H}$ ions were detected and studied.

3. Results and discussion

3.1. Preparation and physicochemical characterization of exfoliated MoSe_2 nanosheets

A straightforward procedure that combined liquid-phase exfoliation via sonication with an organic-to-aqueous phase transfer step was used to obtain MoSe_2 nanosheets or flakes from their bulk precursor that were suitable for the catalytic tests. Briefly, bulk MoSe_2 powder was first delaminated in *N,N*-dimethylformamide (DMF), as a well-known solvent

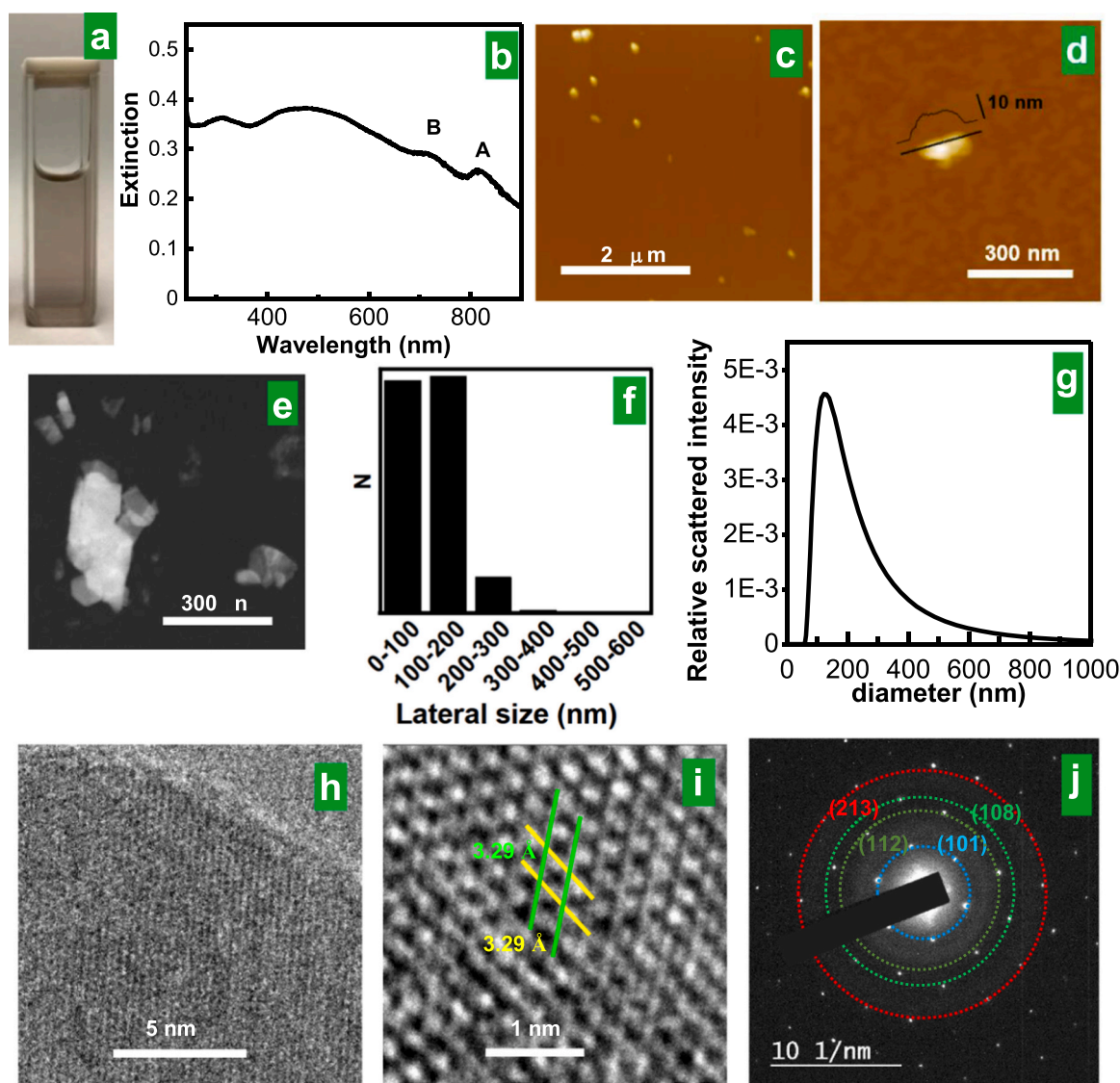


Fig. 1. Characterization of MoSe_2 dispersions. (a) Digital photograph of the MoSe_2 dispersion and the corresponding (b) UV-Vis extinction/adsorption spectrum with indication of the characteristic excitonic peaks. Representative (c,d) AFM and (e) STEM images of the dispersed objects. (f) Histogram of lateral size derived from STEM imaging. (g) Particle size (from hydrodynamic diameter) distribution from DLS measurements. (h,i) Representative HR-TEM images of the MoSe_2 flakes at different magnifications. The parallel lines in (i) assist in visualizing *a* and *b* cell parameters in the hexagonal cell of MoSe_2 lattice. (j) SAED pattern of the MoSe_2 lattice with indication of the family planes involved in the observed diffractions.

for efficient TMD exfoliation [45], by means of bath-sonication. The resulting suspension was centrifuged at a low speed to sediment the non-delaminated and poorly delaminated fractions of the material, with the supernatant containing well-exfoliated flakes. The latter was collected and subjected to several cycles of (i) high speed centrifugation to completely sediment the exfoliated flakes and (ii) re-suspension of the flakes in deionized water by a brief sonication step. Such a procedure finally afforded a visually homogeneous aqueous suspension of MoSe₂ nanosheets (Fig. 1a). Indeed, UV-Vis absorption spectroscopy (Fig. 1b) was consistent with the dispersed material being the thermodynamically stable, 2H phase of MoSe₂, as noticed from the characteristic excitonic peaks of this TMD located at ~720 and 815 nm [45,46]. Atomic force

microscopy (AFM; Fig. 1c and d) and scanning transmission electron microscopy (STEM; Fig. 1e) imaging of the dispersed objects revealed them to exhibit an irregular polygonal profile with lateral size typically between several tens and a few hundreds of nanometers (see STEM-derived histogram in Fig. 1f) and thickness ~10 nm. Considering that the thickness of a MoSe₂ monolayer is ~0.6–0.7 nm [47,48], this implies that individual nanosheets in the aqueous suspension were made up of about 14–17 monolayers. The lateral size distribution determined by STEM for the MoSe₂ nanosheets was corroborated with dynamic light scattering (DLS) measurements. As can be seen in Fig. 1g, the hydrodynamic diameters of the MoSe₂ particles dispersed in water were calculated to be roughly between 70 and 400 nm by this technique.

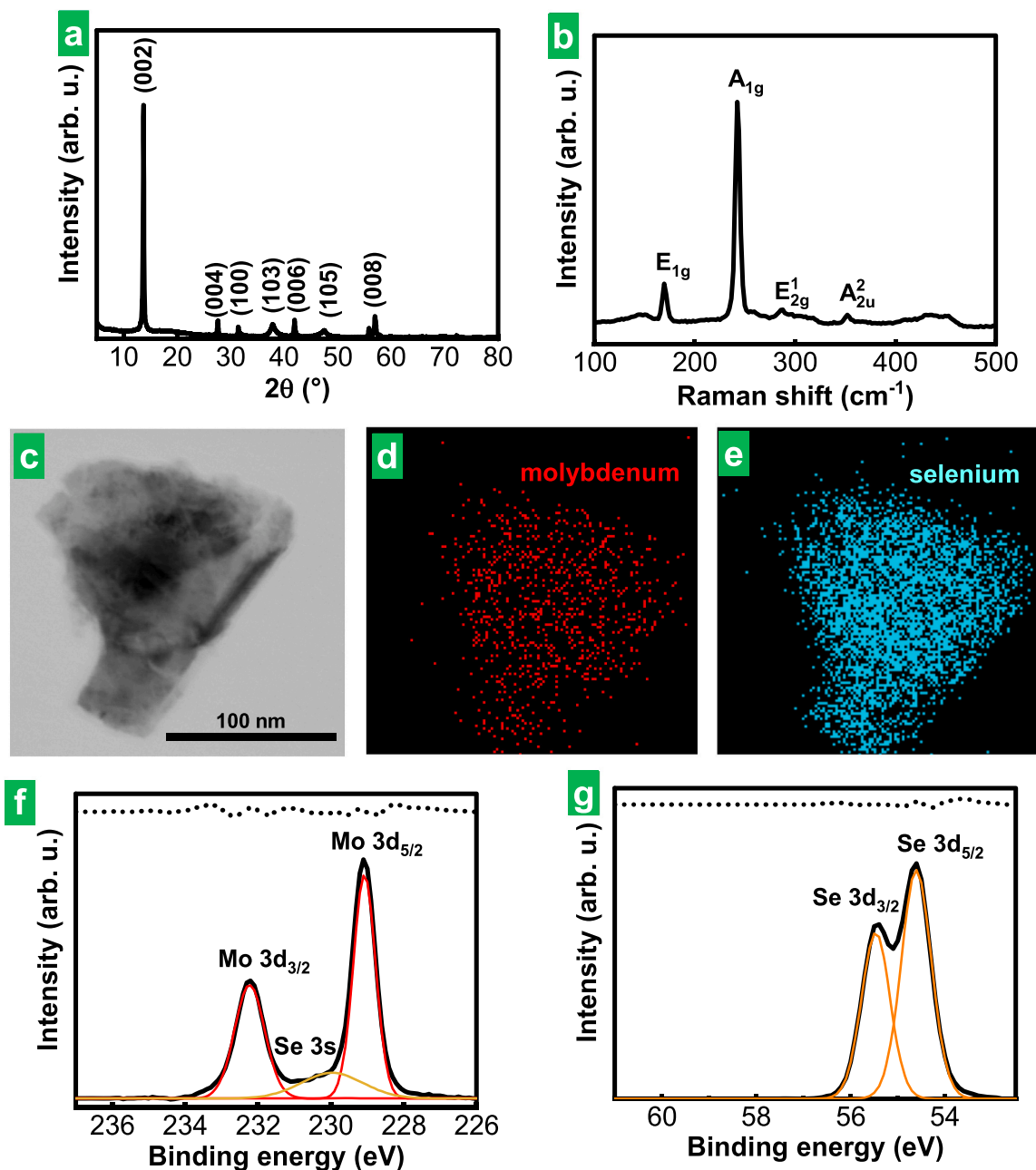


Fig. 2. Structural and chemical characterization of the exfoliated MoSe₂ flakes. (a) XRD diffractogram of exfoliated MoSe₂, where peaks have been labelled according to JCPDS card 29–0914. (b) Raman spectrum for exfoliated MoSe₂ flakes. The main bands have been labeled for clarity. (c) STEM image of exfoliated MoSe₂ and (d,e) the corresponding energy dispersive X-ray (EDX) area mapping of (d) molybdenum and (e) selenium. (f) Background-subtracted, high-resolution XPS Mo 3d (and Se 3s) spectra and (g) Se 3d core level spectrum of exfoliated MoSe₂. The experimental data are graphed with a solid black line while the deconvoluted Mo and Se components are depicted with red and orange traces, respectively. The difference between the experimental and the fitted spectrum is graphed on top of the fitted XPS spectra (dotted traces).

Although the hydrodynamic diameter of suspended particles is obviously correlated to their actual dimensions, such a correlation can be somewhat convoluted due to the different shapes that particles can adopt [49]. For 2D materials like graphene and TMDs, a quantitative relationship between the hydrodynamic diameter and the lateral size of dispersed nanosheets, based on approximating their shape to circular discs, has been previously demonstrated [50]. Using this relationship, the lateral size of the present MoSe₂ nanosheets was estimated from the DLS measurements to be approximately between 40 and 500 nm, which was in reasonably good agreement with the results obtained by direct STEM imaging (Fig. 1f). HR-TEM images [Fig. 1h and Figs. S1a–c in section S1 of the Supplementary Material (SM)] confirm that the exfoliated flakes were multilayer in nature. Atomic resolution images of the basal planes and the corresponding SAED patterns (Figs. 1i and 1j, respectively) reveal their hexagonal symmetry and unit cell parameters.

The structural configuration and chemical make-up and of the exfoliated MoSe₂ flakes were investigated by X-ray diffraction, Raman spectroscopy, energy dispersive X-ray (EDX) mapping and X-ray photoelectron spectroscopy (XPS). XRD confirmed the crystalline structure of the exfoliated flakes to be that of 2H-MoSe₂ (Fig. 2 a) belonging to P6₃/mmc space group (JCPDS card 29-0914), as in the starting MoSe₂ powder (see Fig. S2a). Indeed, the Raman spectra of the exfoliated flakes (Fig. 2b) displayed the characteristic features of 2H-phase MoSe₂ [51], i.e., an intense peak located at ~242 cm⁻¹ (A_{1g} band) together with weaker bands at ~170 (E_{1g}), ~288 (E_{2g}) and ~352 (A_{2u}) cm⁻¹. The position of the A_{1g} (E_{2g}) band has been shown to red (blue)-shift when bulk MoSe₂ is downsized to the few- and single-layer level [52–54]. Hence, the spectral separation between these two bands can be taken as a fingerprint for the presence of 2D nanosheets of this material. However, such a spectral fingerprint is only sensitive to the thinnest nanosheets (<5 monolayers). Indeed, the A_{1g}-E_{2g} separation determined for our MoSe₂ flakes (~4 cm⁻¹, consistently measured at many different spots of the sample) was virtually identical to that obtained for the starting bulk material (Fig. S2b in the SM). This result agreed with the AFM and HRTEM data of the exfoliated product indicating that it was made up of relatively thick nanosheets (~14–17 monolayers, Fig. 1d and S1a–c). As concluded from the EDX area mapping (Fig. 2c–e) and the XPS survey spectrum (Fig. S1d in section S1 of the SM), the material was mainly comprised of Mo and Se in approximately 1:2 at. ratio (really, a little low in chalcogen, as will be explained below). Although a very small amount (<5 at%) of carbon and oxygen elements was also detected, this probably originated from the ever-present adventitious contamination in the XPS analysis chambers [55] (or, in this particular case, from residual adsorbed DMF molecules). The corresponding high resolution, core-level Mo 3d spectrum (Fig. 2f) exhibited the well-known doublet band arising from the 5/2 and 3/2 spin states of this electron energy level. Moreover, the binding energies measured for such states, namely, 229.0 eV for Mo 3d_{5/2} and 232.2 eV for Mo 3d_{3/2}, were consistent with the atomic environment expected for this metal in 2H-phase MoSe₂ (Mo⁴⁺ with trigonal prismatic coordination to the chalcogen) [47,56,57]. A similar conclusion regarding the presence of 2H-phase MoSe₂ was reached from the high resolution core-level Se 3d spectrum (Fig. 2g), that is, the position of the Se 3d_{5/2} (54.5 eV) and 3d_{3/2} (55.4 eV) levels was also in agreement with such a structural attribution [56,57]. Both core-level spectra were essentially identical to those of the starting bulk MoSe₂ powder (see Fig. S2c and d in the SM), suggesting that the material was not altered to any significant extent during its exfoliation and subsequent processing. In particular, no oxidized Mo or Se species could be seen at the levels that can be detected by this technique (i.e., above a few tenths of at%), either in the starting material or its exfoliated counterpart. For instance, no doublet bands arising from MoO_x (232.8 and 236 eV) or SeO_x (59 and 59.8 eV) were noticed [56]. Further details on the XPS characterization of MoSe₂, including an explanation on the assignment of a feature observed in the Mo 3d spectral range to Se 3s core level (see Fig. 2f and Fig. S2c) are given in section S1 of the SM.

The same procedure was applied to prepare aqueous dispersions of exfoliated MoS₂ flakes. Their morphological, structural and chemical characterization (Figs. S3 and S4 in section S2 of the SM) yielded very similar results to those obtained for their MoSe₂ counterpart, i.e., the exfoliated product was made up of submicrometer-sized nanosheets that were several layers thick and retained the original 2H phase of the starting bulk material. The only significant difference between the two exfoliated TMDs concerned their lateral size distribution. While the DLS-derived hydrodynamic diameters for the MoSe₂ and MoS₂ dispersions were essentially identical (see Fig. 1g and S3g), the population of the smallest flakes (< 100 nm) as determined by direct STEM imaging was noticeably larger in the MoSe₂ sample (compare Fig. 1f and S3f). This result was not unreasonable, considering that the Mo-Se bond in MoSe₂ is weaker than its Mo-S counterpart in MoS₂ [58] and, therefore, that MoSe₂ slabs are more likely to fragment into smaller pieces during the sonication treatment. The fact that the DLS measurements did not reflect this difference could have its origin in the relatively weaker scattering of light of the smaller particles in relation to the larger ones, which makes the former more difficult to be detected by this technique.

3.2. Catalytic performance of exfoliated MoSe₂ nanosheets toward nitroarene reduction and comparison with MoS₂

With a view to their use as (unsupported) catalysts for reduction reactions for water treatment and, thus, carried out in water, the colloidal stability of 2D TMD nanosheets in aqueous medium is thought to be critical [59]. The exfoliated MoSe₂ flakes prepared here exhibited a limited colloidal stability in such a medium. Specifically, they showed visible signs of aggregation and sedimentation after their dispersions (concentration ~0.10–0.15 mg mL⁻¹) were allowed to stand undisturbed for a few to several days. However, the material could be readily re-suspended via sonication, to give again visually homogeneous dispersions that remained stable for several hours to a few days. This behavior was not surprising, considering that bare TMDs are in general relatively hydrophobic materials and that the exfoliated MoSe₂ flakes were transferred to pure water without the aid of any surfactants or colloidal stabilizers [45,60–62]. Still, it is also known that different 2D materials, including TMDs like MoS₂ and MoSe₂, possess a small but non-negligible degree of colloidal stability by themselves (i.e., without the assistance of external dispersants) in pure water at moderate to low concentrations [63,64]. This was indeed the case of the present aqueous MoSe₂ dispersions, which remained stable for at least several hours before starting to sediment to any significant extent (quantitative evidence of such stability is provided in the SM, in Section S4 and Fig. S6a, as will be explained below). As a result, a sufficiently long-time window was in practice available for testing the catalytic performance of the bare flakes without the need to resort to surfactants or stabilizers that could interfere with the catalytic reactions [16,65], which allows comparing the intrinsic catalytic activities of MoSe₂ and MoS₂.

The ultimate cause of the non-negligible colloidal stability of some hydrophobic 2D materials in pure water is not yet well understood, but it has been ascribed to the presence of surface charges on the nanosheets [63]. The MoSe₂ flakes obtained here were, in fact, negatively charged in water, exhibiting a zeta potential value of –15 mV that was indicative of dispersions with incipient stability [66]. The latter was in turn consistent with the above observation of aqueous MoSe₂ suspensions that were only stable for several hours to a few days. A similar result was obtained regarding the stability of the aqueous MoS₂ suspensions, the zeta potential of which was measured to be –11 mV. As for the actual chemical species responsible for the negative charges in the bare TMD nanosheets, we believe (polyoxo)metalates to be very plausible candidates, and specifically (polyoxo)molybdates in the case of molybdenum-based TMDs. Small amounts of such negatively charged species are present in bulk TMD powders as a result of natural oxidation processes, although they can also be generated via purposeful oxidation. Moreover, these (polyoxo)metalates have been shown to trigger TMD

exfoliation by an electrostatic repulsion mechanism upon their adsorption on the surface and at interlayer spaces of the TMD particles [67,68]. Consequently, they could furnish the bare exfoliated flakes with negative charges and, therefore, with some degree of colloidal stabilization.

The catalytic activity of the exfoliated MoSe₂ flakes was tested in the reduction reactions of a number of nitroarenes, which were carried out in water at room temperature with NaBH₄ as the reducing agent. NaBH₄ is the reductant of choice for nitroarene reduction [69], being comparatively more stable and safer than other reductants, such as hydrazine, and, in contrast with other hydride-based reductants, such as LiAlH₄ or silanes, compatible with aqueous medium [14], which is essential for its application in water treatment. Specifically, the following substrate molecules were tested: 2-nitrophenol (2-NP), 3-nitrophenol (3-NP), 4-nitrophenol (4-NP), 2-nitroaniline (2-NA), 3-nitroaniline (3-NA), 4-nitroaniline (4-NA) and nitrobenzene (NB). Such reactions are known to be thermodynamically downhill overall, but unless a proper catalyst is used, they cannot proceed at a significant rate at room temperature due to the presence of considerable kinetic barriers [69]. Furthermore, in all these cases the reaction progress was conveniently monitored by means of UV-Vis absorption spectroscopy. This was because the substrate molecules exhibit signature absorption bands at distinct wavelengths that are absent from their reduced counterpart (see Fig. S5 in section S3 of the SM for the corresponding absorption spectra). Hence, such bands can be used to follow the substrate concentration in the

reaction medium on the basis of the Lambert-Beer law, thereby affording kinetic profiles where substrate concentration is plotted against reaction time [25,26]. However, in the present case, derivation of the actual reaction kinetic profiles required applying some corrections to the raw profiles that were obtained from the UV-Vis absorption measurements, where absorbance of the reaction medium at a given wavelength vs. time was recorded. The need for such corrections arose from the observation that the MoSe₂ nanosheets, which contributed to the absorbance of the reaction medium just like the substrate itself, sedimented slowly in the presence of NaBH₄. As a result, the raw kinetic profiles included a time-dependent contribution from the slowly declining absorbance of the catalyst, which had to be removed to arrive at the actual kinetic profile of the tested reaction. Sedimentation of the MoSe₂ nanosheets was most likely due to waning of their colloidal stability in the high ionic strength medium created by the reducing agent (charge neutralization) [66], but it was sufficiently slow so as not to compromise the measurement of their catalytic activity. A detailed account of these effects and the applied corrections is given in section S4 and Fig. S6 of the SM.

Fig. 3 shows actual kinetic profiles (i.e., substrate concentration vs. time) for the reduction of 2-NP, 3-NP, 4-NP and NB (panel a) as well as 2-NA, 3-NA and 4-NA (panel b). These plots do not include the so-called induction period, which was an initial section of constant concentration in the profiles, as it was removed for clarity. Such an induction period is typically observed with both metal-based and MoS₂ catalysts

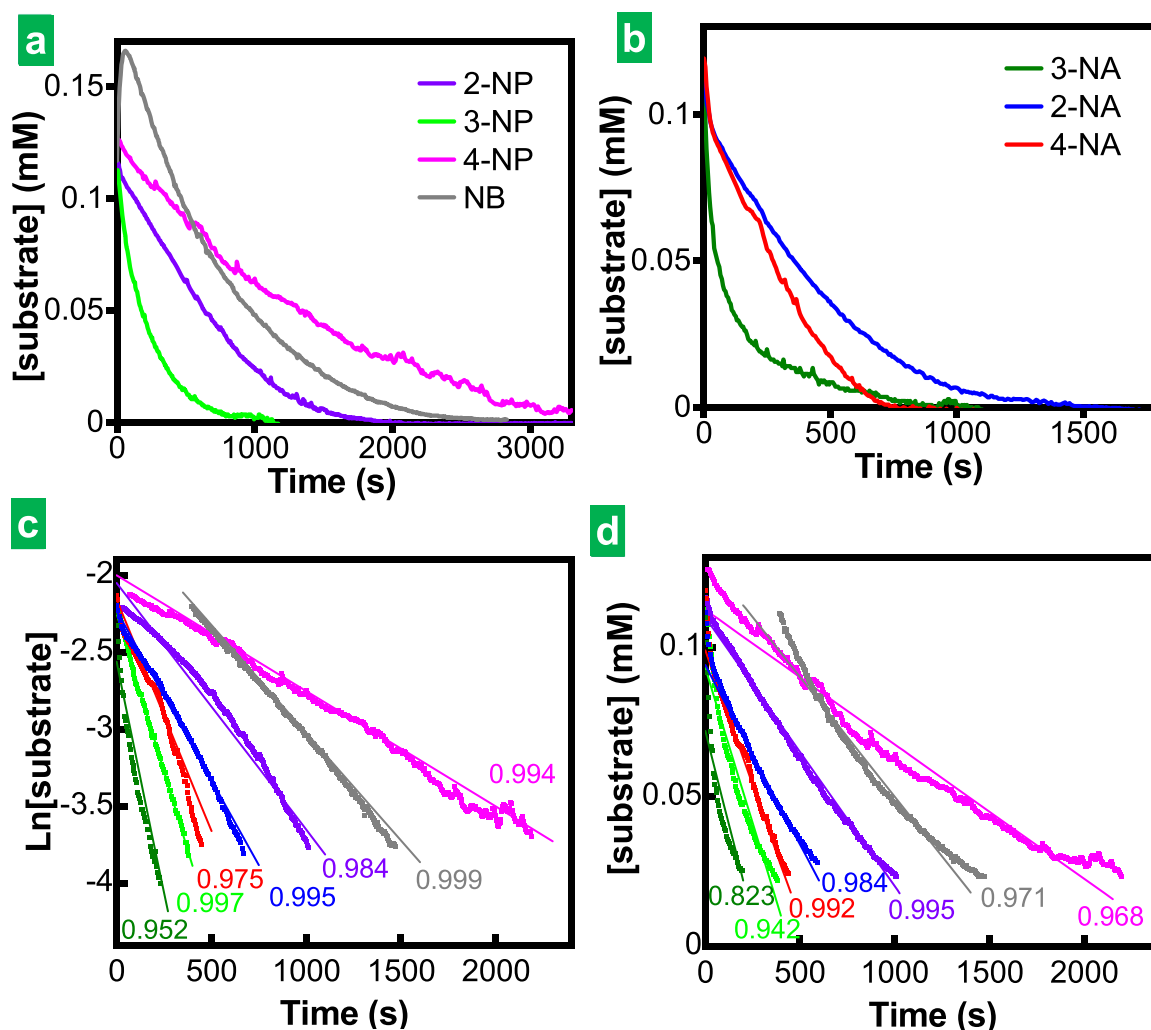


Fig. 3. MoSe₂ nanosheets as catalysts for nitroarene reduction. (a) Substrate concentration vs. time for the reduction of 2-NP (violet trace), 3-NP (light green), 4-NP (magenta) and NB (gray) (b) as well as 2-NA (blue trace), 3-NA (green) and 4-NA (red) using exfoliated MoSe₂ as catalyst. Fitting of the kinetic profiles in (a) and (b) to (c) exponential and (d) linear decay functions using the same color code with indication of the corresponding regression coefficients (R²).

[25,69] and was also regularly seen here with the MoSe₂ nanosheets (see section S4 in the SM). Its origin has been related to conversion of the reaction products (i.e., anilines) back to the starting substrates (nitroarenes) as a result of their catalytic oxidation with oxygen molecules dissolved in the reaction medium [70]. It can be seen from Fig. 3 that a plateau at substrate concentration close to zero was reached upon reaction completion in all cases, indicating that essentially full conversion of the reactants was attained. Moreover, the reaction profiles seemed to follow non-linear decay functions, which revealed information on the reaction order and thus on the kinetics of these processes. To address this question in detail, we first note that the kinetic profiles measured for the catalytic reduction of nitroarenes generally obey either a first-order or a zero-order behavior with respect to the substrate concentration [25,26,69,71]. In other words, the profiles obey one of the two following rate equations:

$$\text{First-order behavior (reaction order of 1)} \quad d[S]/dt = -k_1[S] \quad (1)$$

$$\text{Zero-order behavior (reaction order of 0)} \quad d[S]/dt = -k_0 \quad (2)$$

, where $[S]$ is the substrate concentration at time t , and k_1 and k_0 are the apparent reaction rate constants. Eqs. (1) and (2) do not explicitly incorporate the concentration of the other reactant (i.e., NaBH₄) on their right-hand side. Because the reducing agent was used in a very large excess compared to the amount of substrate, its concentration could be reasonably assumed to remain constant during the reduction reaction, and so the corresponding term was implicitly included in the rate constants (rigorously speaking, we should use the terms pseudo-first-order and pseudo-zero-order). Further, these equations indicate that the kinetic profiles of first-order and zero-order reactions are described by exponential and linear decay functions, respectively. Therefore, to determine which of these two reaction orders best replicated the actual reduction kinetics of the substrate molecules, we fitted their measured kinetic profiles to both exponential and linear decay functions, and determined their corresponding regression coefficient (R^2) as an indicator for the quality of the fit. The results are shown in Fig. 3c and d for the exponential and linear fits, respectively. Overall, exponential decay functions reproduced the experimental profiles better than their linear counterparts, with R^2 values of 0.952–0.999 compared to 0.823–0.995 for the linear fits.

The kinetic behaviors observed here with the 2D MoSe₂ catalyst differed from those recently reported for MoS₂ nanosheets functionalized with acetic acid groups, where a correlation between reaction order and net electric charge of the substrate in the reaction medium was noticed overall [26]. More specifically, negatively charged (electrically neutral) substrate molecules tended to exhibit first (zero) order kinetics. Such trends were rationalized by assuming that the reaction rate was heavily influenced by the rate of diffusion of the substrate molecules to the active sites on the surface of the catalyst. Negatively charged molecules would experience a substantial electrostatic repulsion barrier when approaching the surface of the acetic acid-functionalized MoS₂ nanosheets (zeta potential of about −40 mV at a pH similar to that of the reaction medium, i.e., 10–11, and −25 mV at pH 4), and so their diffusion to the catalytic active sites would be significantly restricted. As a result, the corresponding reduction rates can be expected to be directly proportional to the substrate concentration [Eq. (1)], giving first-order kinetics. On the other hand, no electrostatic repulsion barriers would be in place for neutral molecules, so their unrestricted access to the catalytic active sites could easily make the latter to become saturated. Hence, the corresponding reduction rates would be essentially independent of substrate concentration [Eq. (2), zero-order kinetics]. However, this interpretation did not hold for the present MoSe₂ nanosheets, because 2-NP, 3-NP and 4-NP were negatively charged in the reaction medium (pK_a values around 7–8, i.e., these species were in the form of nitrophenolates), whereas 2-NA, 3-NA, 4-NA and NB were electrically neutral (pK_a values of the conjugate acids of the nitroanilines below 3) [72], but all the substrate molecules exhibited a similar kinetic behavior

(i.e., first-order kinetics). Here, it is reasonable to argue that the overall negative charge on the MoSe₂ nanosheets is too small (zeta potential less negative than that of acetic acid-functionalized MoS₂) to sustain any substantial repulsion barrier against negatively charged molecules. Hence, essentially unrestricted access to the active sites would be expected with any substrate molecules, regardless of their net electrical charge. Nevertheless, this should have led to zero-order kinetics for both negatively charged and neutral substrates, but not to the first-order behavior that was actually observed with the MoSe₂ catalyst. Clearly, other factors should be contributing decisively to the kinetics of the latter besides the rate of diffusion of the substrate molecules to the catalytic active sites.

With the aim of shedding light on this issue, the kinetic profiles of nitroarene reduction were also recorded using, as the catalyst, the MoS₂ nanosheets prepared here in an analogous way to the MoSe₂ flakes. Remarkably, the measured profiles (Fig. 4a and b) were all seen to be clearly linear with this MoS₂ catalyst. Such a conclusion was quantitatively supported by the corresponding fits, which were rather good (R^2 values of 0.992–0.998) for the linear decay fits, but very poor (R^2 values of 0.962–0.988) for their exponential counterparts. This would be indeed the expected result for a MoS₂ catalyst that displays a fast diffusion of substrate molecules to the active sites, as discussed above, and therefore where such diffusion is not restricted by electrostatic barriers. Considering that the overall negative charge of the present MoS₂ flakes was substantially smaller than that of the acetic acid-functionalized nanosheets, the kinetic behaviors observed for these two types of 2D MoS₂ catalyst were totally consistent with each other. However, both the MoS₂ and MoSe₂ nanosheets prepared here were similarly charged in aqueous medium (similar zeta potential values), but their kinetic behaviors clearly differed. This observation suggested again that substrate diffusion to the active sites could not be the only determinant factor of the behavior noticed for the MoSe₂ catalyst. As discussed in the following, we believe that such kinetic discrepancies between MoSe₂ and MoS₂ arise from differences in the intrinsic activity of their catalytic sites.

3.3. Rationalizing the kinetic behavior of nitroarene reduction with MoSe₂ and MoS₂ catalysts

To rationalize the factors that govern the kinetic behavior of nitroarene reduction with the TMD catalysts, we note that the reaction rate (i.e., $d[S]/dt$) can be regarded to be proportional to the degree of surface coverage of the catalytic active sites by both the substrate, $\theta_s(t)$, and the reducing agent, $\theta_r(t)$, based on a Langmuir-Hinshelwood analysis [71]. Because the amount of NaBH₄ was much larger than that of the nitroarenes and its concentration could be assumed to remain constant throughout the reaction, to a first approximation $\theta_r(t)$ was also assumed to be constant with time. On the other hand, $\theta_s(t)$ was expected to depend mainly on two factors: (i) the rate of diffusion of the substrate molecule to the active site for adsorption, and (ii) the rate at which the substrate molecule adsorbed at the active site is converted to its corresponding product and the product is desorbed from the active site. More specifically, and for the sake of simplicity of the argument, factor (i) can be associated to a characteristic time, t_{unocc} . This can be seen as the time it takes for an active site to be occupied again by a substrate molecule after the reaction product from a previous reaction desorbs from that active site. The higher the diffusion rate of the substrate molecules to the active sites, and particularly the higher their concentration in the reaction medium, the shorter t_{unocc} should be. In turn, factor (ii) can be associated to a characteristic time t_{occ} , which would be the time it takes for the adsorbed substrate molecule to be converted to the reaction product plus the time it takes for the reaction product to desorb from the active site. Here, the higher the efficiency of the active sites in churning out reaction products, the shorter t_{occ} should be. Then, $\theta_s(t)$ would be dictated by t_{unocc} and t_{occ} through the following relation:

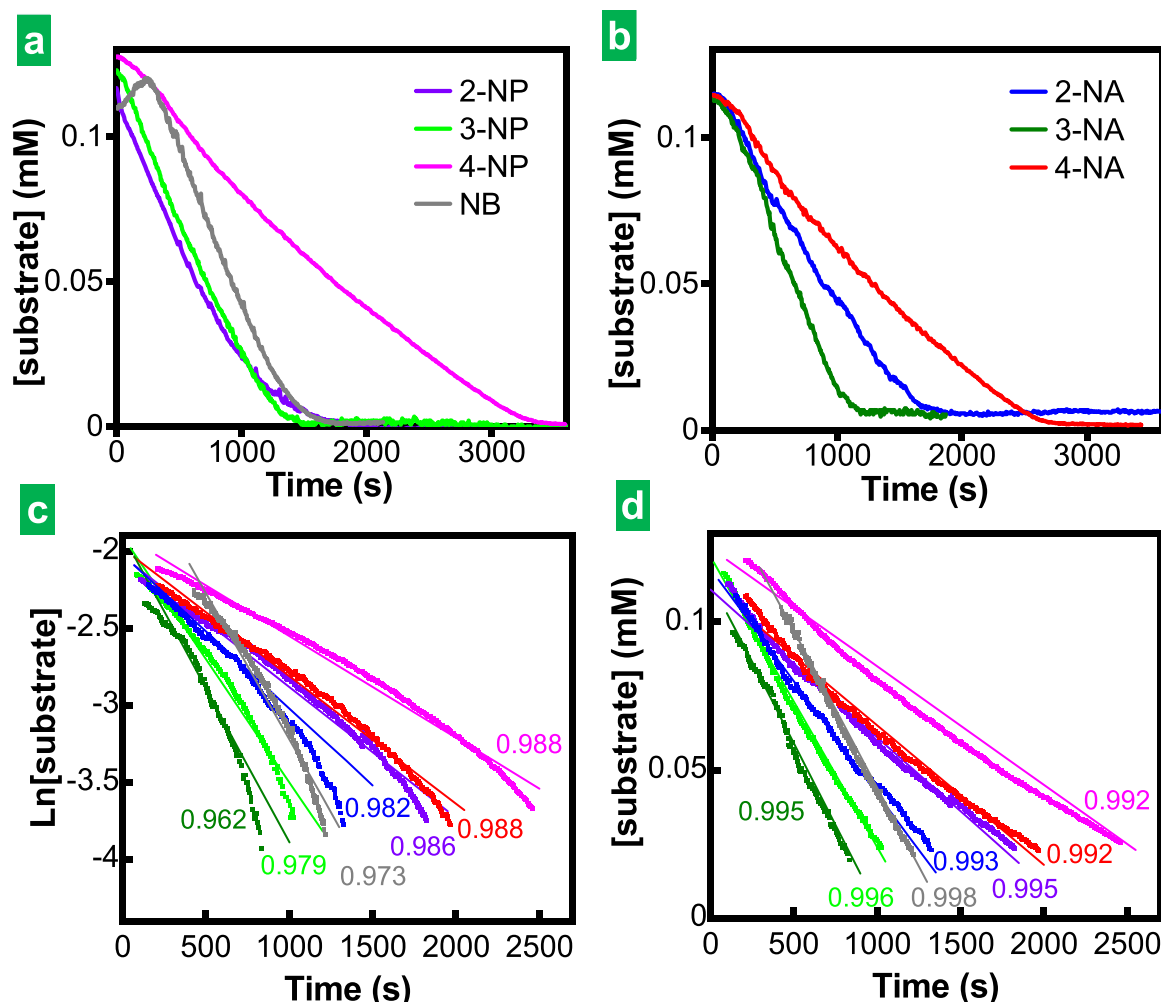


Fig. 4. MoS₂ nanosheets as catalysts for nitroarene reduction. (a) Substrate concentration vs. time for the reduction of 2-NP (violet trace), 3-NP (light green), 4-NP (magenta) and NB (gray) (b) as well as 2-NA (blue trace), 3-NA (green) and 4-NA (red) using exfoliated MoS₂ as catalyst. Fitting of the kinetic profiles in (a) and (b) to (c) exponential and (d) linear decay functions using the same color code with indication of the corresponding regression coefficients (R^2).

$$\theta_s(t) \propto \frac{t_{occ}}{t_{occ} + t_{unocc}} \quad (3)$$

From Eq. (3), we can make some predictions about the determinants of the reaction order for nitroarene reduction with the different TMD catalysts. First, if access of the substrate molecules to the active sites is essentially unrestricted (i.e., very fast) and the reaction is limited by the substrate-to-product conversion and/or product desorption, then $t_{occ} \gg t_{unocc}$ for most of the reaction (this inequality could not hold anymore after most of the substrate has been consumed). Hence, $\theta_s(t)$ and the reaction rate should be largely constant in time, yielding zero-order kinetics. We infer that such a situation applied in the case of the MoS₂ flakes prepared here (Fig. 4). We note that the fitting of the kinetic profiles in Figs. 3 and 4 were done below 80% substrate conversion, excluding the final stretch, where zero-order kinetics would not hold. Second, a different scenario could be envisaged for a MoS₂ catalyst where the value of t_{occ} was essentially the same as that of the previous case (i.e., same material and thus same type of active sites), but where t_{unocc} was comparable in magnitude to t_{occ} due to a substantial barrier to diffusion of the substrate molecules to the catalyst. In this case, $\theta_s(t)$ and the reaction rate would both decrease (in absolute value) as the reaction progressed, because t_{unocc} would become progressively larger relative to t_{occ} as the substrate was being consumed. This situation would be compatible with a first-order reaction and was that observed for the acetic-acid functionalized MoS₂ nanosheets in the reduction of negatively charged nitroarenes. Third, for the present MoSe₂ nanosheets it is

reasonable to assume that substrate diffusion to the active sites was unrestricted, yielding t_{unocc} values similar to those of their MoS₂ counterpart (both TMDs prepared here displayed very similar zeta potential values). If t_{occ} for MoSe₂ were also similar to that of MoS₂, then the former catalyst would be expected to exhibit zero-order kinetics as well in the reduction of nitroarenes. However, this was not the case and first-order kinetics was observed instead (Fig. 3). In consequence, for MoSe₂ to exhibit first-order behavior, we have to assume that its t_{occ} values were substantially smaller than those of MoS₂, which in turn implies that the catalytic sites of MoSe₂ are intrinsically more active than those of MoS₂. It should be noted that in this discussion t_{unocc} and t_{occ} are not uniquely defined quantities, because the processes they describe are obviously stochastic in nature and, therefore, should be better characterized by a distribution of time intervals where such processes can occur. However, the essence of the physicochemical factors that dominate the catalyzed reactions could already be captured by this simplified treatment. Indeed, a more rigorous treatment involving the rate constants of the individual processes, i.e., substrate adsorption onto the active site, substrate conversion to product and product desorption, led to similar conclusions (see section S5 in the SM).

To test the prediction that MoSe₂ nanosheets are intrinsically more efficient as nitroarene reduction catalysts than their MoS₂ counterpart, their catalytic activities were quantitatively compared. Such activities were evaluated in terms of moles of substrate converted per unit time per mole of TMD catalyst. We note that the catalytic sites are thought to

be associated to coordinatively unsaturated molybdenum atoms located at structural defects in the TMD lattice, such as edges and chalcogen vacancies [25,29,33].

The presence of chalcogen vacancies as an intrinsic feature of both natural and synthetic TMDs is a result of their relatively low formation energy (~ 2 eV [73]), while the primary cause of their formation lies in solid-gas phase thermodynamic equilibrium, which both the chalcogen and the Mo element tend to reach [73]. Owing to the higher saturated vapor pressure of the chalcogen atom, both MoS_2 and MoSe_2 release more chalcogen than Mo atoms into the gas phase and thus the corresponding TMD is prone to be deficient in the chalcogen element [73]. In the case of MoS_2 , the role of the chalcogen vacancies as catalytically active sites has been explicitly shown by purposefully generating sulfur surface vacancies in the lattice and measuring faster reaction rates in the resulting modified catalysts [25]. To demonstrate that the same behavior also applied in the case of the MoSe_2 nanosheets, selenium vacancies were generated in the latter via a reductive treatment with hydrazine (see section 2.3). The increased fraction of coordinatively unsaturated molybdenum atoms in the MoSe_2 lattice was confirmed by electron paramagnetic resonance (EPR) spectroscopy. Fig. 5a (black trace) shows the EPR spectrum of the starting bulk MoSe_2 powder, which already exhibited a non-negligible signal at a magnetic field of ~ 3150 G [74,75] that indicated the presence of a certain amount of edges and vacancies in this material. After exfoliation of the bulk powder into nanosheets, a significantly stronger EPR signal was recorded (red trace in Fig. 5a), which most likely reflected the increased fraction of edges with unsaturated atoms in the MoSe_2 material that resulted from its downsizing. Upon hydrazine treatment, a further increase in the EPR signal was noticed (blue trace), which could be ascribed to new unsaturated molybdenum centers generated with the selenium vacancies. As anticipated, the catalytic activity of the hydrazine-treated MoSe_2 nanosheets was enhanced compared to that of their untreated counterpart. Such an enhancement became apparent by comparing the corresponding kinetic profiles for different nitroarene reduction reactions (Fig. 5b; dotted traces: untreated nanosheets; solid traces: hydrazine-treated nanosheets), where the hydrazine-treated catalyst clearly afforded faster reduction rates.

Table 1 compares the catalytic activities of the MoSe_2 and MoS_2 nanosheets for the different nitroarene reduction reactions, relative to the number of moles of TMD catalyst in the reaction medium. The catalytic activity values, which were calculated at 80% of substrate conversion, were in general substantially higher for the MoSe_2 nanosheets, demonstrating that this TMD outperformed MoS_2 as a nitroarene reduction catalyst. Further indication of the higher efficiency of MoSe_2 in these reactions was obtained from the observation of shorter induction periods with this catalyst compared to MoS_2 (see Fig. S7 in section S6 of the SM). As the induction period is related to consumption of

Table 1

Comparison of the catalytic activities of the MoSe_2 and MoS_2 nanosheets for the different nitroarene reduction reactions relative to the number of moles of TMD catalyst in the reaction medium. The values are calculated at 80% of substrate conversion.

substrate	MoSe_2 (h^{-1})	MoS_2
2-NP	6.4	2.2
3-NP	15.6	4.0
4-NP	3.0	1.7
2-NA	5.5	2.9
3-NA	15.4	4.1
4-NA	8.8	1.9
NB	4.2	3.0

oxygen dissolved in the reaction medium by catalytic oxidation of the reduced products (i.e., anilines) back to the starting substrates (nitroarenes) [70], a higher turnover rate of reduction products at the active sites of the TMD catalyst should imply a faster consumption of the dissolved oxygen and thus a shorter induction period.

While working with bare TMD flakes in water was useful to compare their intrinsic catalytic activity, this was not the optimal preparation to maximize their performance. In fact, we note that the current research was not focused on finding unprecedented catalytic activities per se, but on providing a rational framework to understand the differences between TMD catalysts. However, it is to be expected that the underlying higher intrinsic activity of MoSe_2 will lead to better catalytic performances than those of MoS_2 applying similar preparation protocols to both TMDs. In fact, just by a simple treatment with hydrazine (see Fig. 5b), the catalytic activities of MoSe_2 for 3-NP and 3-NA reduction approximately doubled ($\sim 30 \text{ h}^{-1}$), yielding activity values which are competitive for non-noble metal catalysts [25,26].

As regards the origin of the higher catalytic activity of MoSe_2 , there are in principle two possibilities that could account for it. The first one concerns the adsorption of the nitroarenes on the active sites of the catalyst. For MoS_2 and other catalysts, it has been shown that the strength of adsorption of the nitroarenes and their intermediate products determines the magnitude of the reaction kinetic barriers and, therefore, the turnover rate of reduction products [76,77]. Because the adsorption strength of nitroarenes at the active sites of MoSe_2 and MoS_2 can be expected to differ somewhat as a result of their slightly different chemical nature, the turnover rates afforded by the two catalysts should also differ. While this possibility cannot be ruled out, we note that the higher activity of MoSe_2 was not restricted to the reduction of nitroarenes, but also included the reduction of species other than the nitro group. For example, the reduction of methyl orange and the hexacyanoferrate anion was faster with the MoSe_2 nanosheets than with

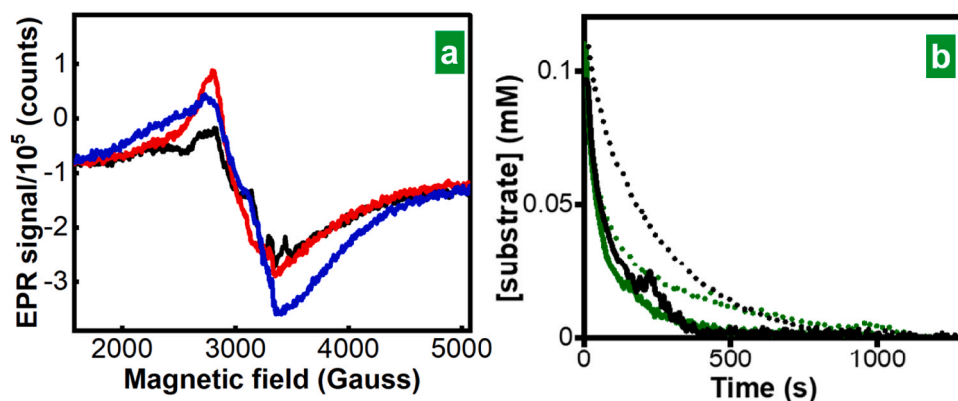


Fig. 5. Characterization of the hydrazine-treated MoSe_2 nanosheets. (a) EPR spectrum of the starting bulk MoSe_2 powder (black trace), and exfoliated MoSe_2 as obtained (red trace), and after hydrazine treatment (blue trace). (b) Kinetic profiles for 3-NA (black traces) and 3-NP (green traces) reduction reactions catalyzed by untreated (dotted traces) and hydrazine-treated MoSe_2 flakes (solid traces).

their MoS₂ counterpart (Fig. S8 in section S7 of the SM), suggesting that the distinct performance of the two catalysts was dictated by more general factors that do not involve the specifics of the substrate molecules.

The second possibility is thus not related to the substrate molecule itself, but to the other reagent taking part in the reaction, namely, the reducing agent NaBH₄ and more specifically the hydride ion (H⁻). We have recently proposed that nitroarene reduction by NaBH₄ with MoS₂ catalysts proceeds via hydrolytic decomposition of the BH₄⁻ anion to give hydride ions [25]. The generated H⁻ species are stabilized at coordinatively unsaturated molybdenum atoms present at sulfur vacancies and edges (but not on the pristine basal surface of the MoS₂ lattice) [78], where they become available for transfer to nitroarene molecules adsorbed at nearby sites, triggering their sequential reduction [25]. Because the stabilization of the hydride ion on the unsaturated molybdenum centers implies the reduction of such centers, it is reasonable to argue that the higher the propensity of these molybdenum centers to be reduced, the higher the abundance of hydrides on the TMD surface available for nitroarene reduction. As a result, higher turnover rates of reduction products should be expected. In turn, the reducibility of the active molybdenum centers should be modulated by their chemical environment, and particularly by the electronegativity of the chemical species bound to the molybdenum atoms. More specifically, the lower the electronegativity of such chemical species, the higher the propensity of the molybdenum centers to be reduced. Considering that selenium is less electronegative than sulfur, we infer that hydrides are more abundantly formed on the molybdenum centers of MoSe₂ compared to those of MoS₂, leading to a higher catalytic activity in the former TMD.

The above interpretation of the role of hydrides in nitroarene reduction with MoSe₂/MoS₂ catalysts is supported by very recent work on the electrocatalytic activity of molybdenum-based materials (oxides, sulfides, alloys, etc) toward the HER [79]. Such an activity was also concluded to rely on the generation of hydrides at reducible Mo⁴⁺ centers present on exposed locations of the material, such as sulfur vacancy defects in the case of molybdenum sulfides. Moreover, a negative correlation between the electronegativity of the chemical species bound to molybdenum and the HER activity was found, suggesting that propensity toward hydride formation is heavily influenced by the reducibility of the Mo⁴⁺ sites. As a proxy for electronegativity of the partner chemical species, the binding energy of Mo⁴⁺ 3d electrons determined by XPS was used (higher binding energy indicating higher

electronegativity). In our case, the lower electronegativity of selenium in MoSe₂ relative to sulfur in MoS₂ was confirmed by the lower binding energy of the Mo⁴⁺ 3d electrons in the former TMD (compare Fig. 2f and S4f, further details are given in the text in section S1 in the SM), thus pointing to a higher propensity of the active molybdenum centers in MoSe₂ toward the formation of hydrides. While molybdenum selenides were not specifically included in that HER work (only sulfides were contemplated among the chalcogenides) [79], it is known from other studies that MoSe₂ is more active than MoS₂ as HER electrocatalyst [80, 81], thus agreeing with the proposed interpretation. A schematic representation of the different propensities of MoSe₂ and MoS₂ to form hydrides on their active molybdenum centers, leading to different catalytic activities for nitroarene reduction, is shown in Fig. 6. We also note that this interpretation provides a rationale to understand the higher catalytic activity toward nitroarene reduction that has been reported for 1T-phase MoS₂ nanosheets relative to their 2H-phase counterpart [13, 21,24]. Because the octahedral coordination of the metal in the 1T phase leads to a binding energy of the Mo⁴⁺ 3d electrons lower than that of the 2H phase (trigonal prismatic coordination) [13], the active molybdenum centers in the former should be more easily reducible, thus giving rise to a higher abundance of hydrides and so to a higher catalytic activity.

It is noteworthy that nitroarene reduction in the presence of MoSe₂ did not show any progress when reductants such as hydrazine monohydrate or ascorbic acid (vitamin C), which involve the generation of hydrogen rather than hydrides, were used instead of NaBH₄. Most probably, as suggested by previous reports [29,31], higher hydrogen pressures would be required for catalytic transfer hydrogenation to occur to a significant extent.

3.4. Computational insight into the catalytic activity trends of MoSe₂ toward nitroarene isomers and possible reaction pathways

The observed differences in catalytic activity between MoSe₂ and MoS₂ toward the investigated reduction reactions were largely attributed, as discussed above, to the distinct availability of reducing hydrides on the surface of these two TMDs. However, we also observed differences in the reduction rate of different nitroarenes, and particularly different isomers of a given nitroarene, with the same TMD catalyst. This was especially the case of the nitroaniline isomers with MoSe₂ (Fig. 3b), where the reduction rate of 3-NA was measured to be significantly

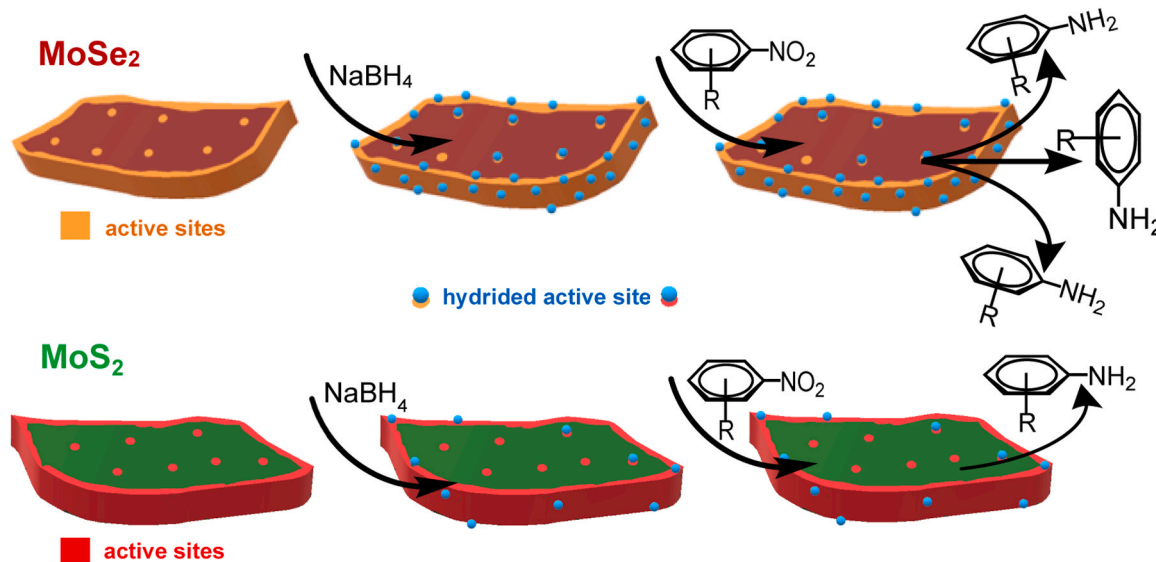


Fig. 6. Different propensities of MoSe₂ and MoS₂ nanosheets to form hydrides. Schematic representation of MoSe₂ and MoS₂ nanosheets and their different propensities to form hydrides on their active sites (chalcogen vacancies and edges), leading to different catalytic activities for nitroarene reduction.

(~2–3 times) faster than that of both 2-NA and 4-NA. Obviously, differences in hydride availability could not be invoked to explain this result, which most likely is originated from the specifics of isomer adsorption at the catalytic active sites of MoSe₂. Therefore, to shed light on this issue, we explored by means of DFT calculations the adsorption of 2-NA, 3-NA and 4-NA on the active sites of the catalyst, modeled as unsaturated molybdenum centers associated to selenium vacancies. Models with one selenium vacancy (1 V_{Se}) and four selenium vacancies (4 V_{Se}) per supercell were considered (see section 2.6 for details of the calculations). In the 4 V_{Se} model, the missing atoms were not adjacent to each other in the selenium atomic plane, but rather second nearest neighbors. Following a prior study of 3-nitrostyrene adsorption on the active sites of WS₂ [33], three configurations of adsorbed nitroanilines were analyzed, which were referred to as *vertical1* (nitro group over a vacancy), *vertical1b* (amino group over a vacancy) and *horizontal* (nitroaniline molecule parallel to the TMD surface). Each adsorption configuration was used for each of the three nitroaniline isomers. Graphical representations of the optimized geometries for 3-NA on the 1 V_{Se} model are shown in Fig. 7(a: *vertical1*; b: *vertical1b*; c: *horizontal*). The calculated adsorption energies, E_{ads} , for the three isomers on the

1 V_{Se} and 4 V_{Se} models are shown in Fig. 7d. E_{ads} values were calculated as $E_{\text{ads}} = E(\text{molecule-surface}) - E(\text{surface}) - E(\text{molecule})$.

For the 1 V_{Se} case, adsorption was favored for the *horizontal* and *vertical1b* configurations, with E_{ads} values around −0.10 eV, but not for the *vertical1* configuration (E_{ads} in the range of 0.5–1 eV). For the 4 V_{Se} model, adsorption was favored for the three isomers in the three configurations, except in the *vertical1* configuration for 2-NA. Indeed, the most notable changes observed in this model relative to its 1 V_{Se} counterpart corresponded to the *vertical1* configuration, which in the case of 3-NA made it to be the most energetically stable. Moreover, the *vertical1* configuration was the only one that led to MoSe₂-molecule distances (specifically, molybdenum-oxygen distances) short enough so as to consider the adsorption process a chemisorption. On the other hand, in the other two configurations the molecules remained practically unchanged, so the adsorption process was classified as a physisorption. In the *vertical1* configuration, one of the oxygen atoms from the nitro group bound to two unsaturated molybdenum atoms from the vacancy, while the other oxygen atom bound to a third unsaturated molybdenum, with the three metal atoms forming a triangle. The nitro group could be then considered to act as a μ_3 bridging ligand by way of $\mu_2 + \mu$ oxygens. The

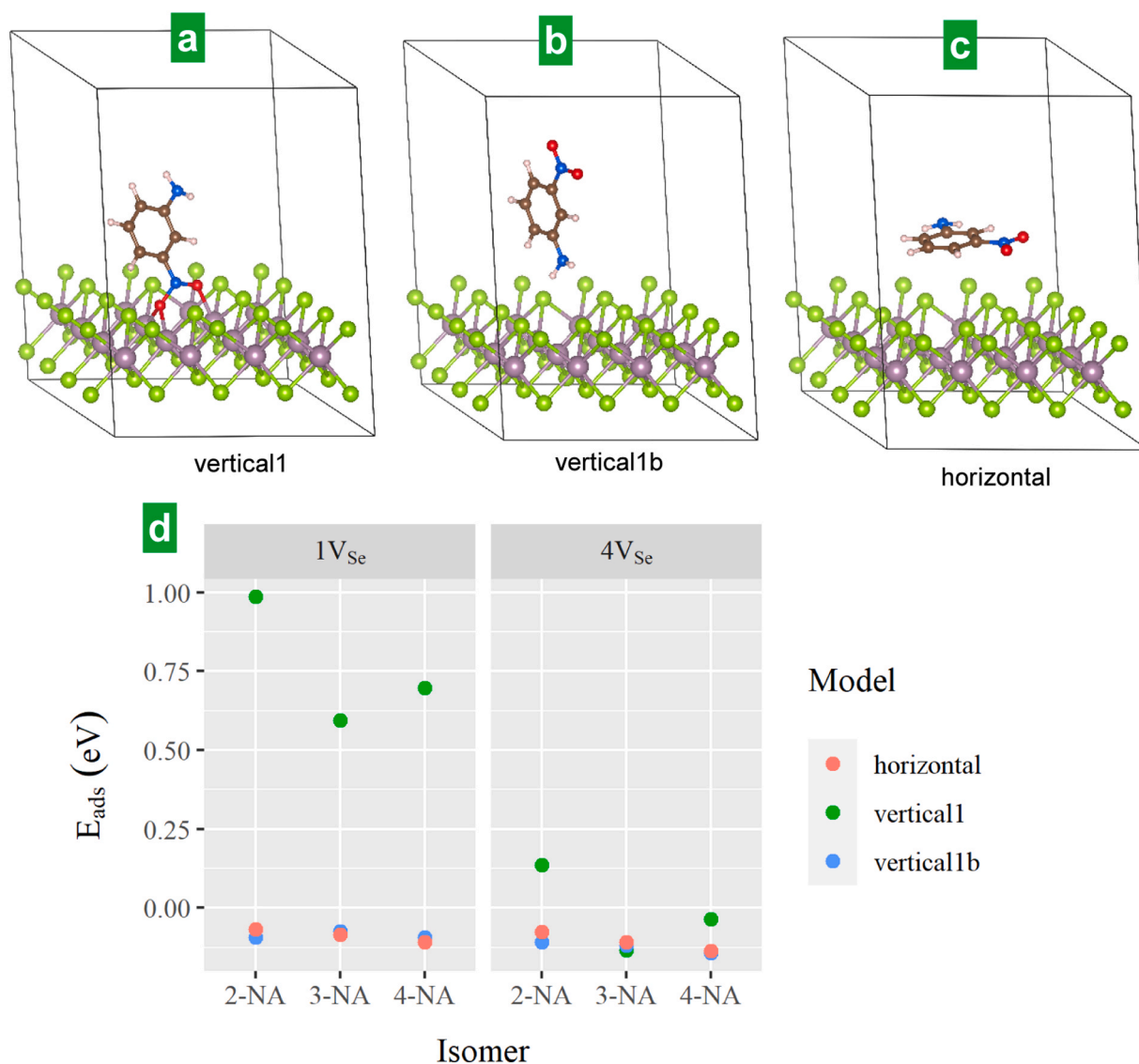


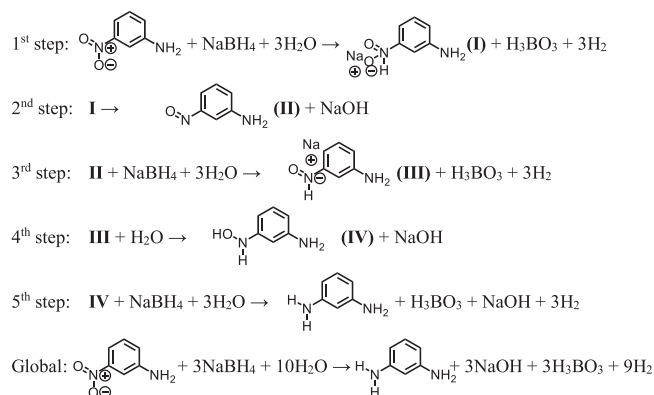
Fig. 7. Energies for the adsorption of the three structural isomers of nitroaniline (NA) on MoSe₂ catalyst calculated for different adsorption geometries. (a–c) Graphical representation of the three studied adsorption geometries, designated as: (a) *vertical1*, (b) *vertical1b*; (c) *horizontal*. (d) Calculated adsorption energies for the three structural isomers of nitroaniline on MoSe₂ catalyst with one (1 V_{Se}) and four selenium vacancies (4 V_{Se}) per supercell and for the three adsorption geometries shown in (a–c).

oxygen-molybdenum and oxygen-nitrogen distances in the adsorbed complex were in the 2.13–2.31 Å and 1.31–1.41 Å range, respectively. The 4 V_{Se} model afforded in general longer oxygen-molybdenum distances and shorter, more symmetrical oxygen-nitrogen bonds than those of the 1 V_{Se} model. Interestingly, the carbon-nitrogen bond distance was also shorter in the 4 V_{Se} case. That is, higher vacancy densities greatly improved the adsorption energetics of the *vertical1* configuration not because of stronger (shorter) $MoSe_2$ -molecule bonds, but by allowing stronger bonding in the nitro group within the molecule. This led to a better energetic balance between the $MoSe_2$ -molecule and the intramolecular interactions.

Because clustered chalcogen vacancies in TMDs are generally more stable than isolated, single vacancies [82,83], the 4 V_{Se} model was regarded as a more realistic representation of the active sites of $MoSe_2$ than the 1 V_{Se} model. Moreover, selenium vacancies in very close proximity to each other would be needed to secure a supply of reducing hydrides to a nitroarene molecule adsorbed at a given vacancy site. Thus, if we consider the average adsorption energies for the three configurations in 4 V_{Se} (see Fig. 7d), we conclude that adsorption should be favored for 3-NA compared to the other two isomers. Such a preference of the active sites toward 3-NA was even more apparent when considering the *vertical1* configuration alone. The latter is expected to be the most favorable configuration for reduction of the nitroaniline, as the nitro group would be particularly accessible to nearby adsorbed hydrides. As a result of this, we would expect the reduction of 3-NA to be the fastest among the three nitroaniline isomers, which agrees with the experimental observations (Fig. 3b). We note that the slightly higher propensity of 3-NA to chemisorb at the selenium vacancies was largely due to energy differences between the nitroaniline isomers as isolated molecules, i.e., without taking their interaction with $MoSe_2$ into account. Specifically, 2-NA and 4-NA are more stable than 3-NA owing to the extra delocalization of the amino lone pair over the nitro group in the resonance hybrid, and this implied an energy penalty when the former two isomers were adsorbed on the vacancy-decorated TMD surface. Still, a difference in adsorption strength between 2-NA and 4-NA was noticed in Fig. 7d (more favorable for 4-NA), which was actually reflected in the experimental results (Fig. 3b). This difference comes from the close proximity of the nitro and amino groups in 2-NA, which provides extra stabilization of the isolated molecule resulting from intramolecular hydrogen bonding. Such an extra stabilization could in principle be compensated for upon adsorption of 2-NA if both the nitro and amino groups, and not just the nitro group, were able to efficiently interact with unsaturated molybdenum atoms from selenium vacancies. However, in the 4 V_{Se} model the selenium vacancies were not strictly adjacent to each other, which made the simultaneous adsorption of both chemical groups difficult, due to steric hindrance. Therefore, to explore this possibility, we calculated the adsorption energy of 2-NA on a $MoSe_2$ model with adjacent vacancies, specifically, two double vacancies per supercell (to preserve a total of four missing selenium atoms as in the case of 4 V_{Se}) (see Figs. S9a and S9b, section S8, of the SM). As anticipated, the double vacancies allowed for the simultaneous adsorption of the nitro and amino groups while preserving the intramolecular hydrogen bond, with the corresponding configuration being referred to as *vertical1c* (see Fig. S9c, section S8, of the SM). The calculated E_{ads} value for this 2-NA configuration was very close to that of the *vertical1* configuration for 4-NA in the 4 V_{Se} model (see Fig. S9d), and still lower than that of 3-NA. However, we note that, at least in the case of MoS_2 , adjacent vacancies are generally unstable and transform quickly into alternating patterns of chalcogen atoms and vacancies [84]. Thus, presumably *vertical1c* configuration will be unlikely, and *vertical1* configuration will determine the reaction progress, in agreement with the experimental observations.

To clarify the role of the catalyst, we also calculated the energies associated to the reaction intermediates for the reduction of 3-NA along a mechanism similar to that proposed by Bae et al. for 4-NP reduction by $NaBH_4$ with magnetite (111) surface as the catalyst [85]. Following their

approach, we compared the energies of the different intermediates in the presence and absence of the catalyst. Initially, the following five steps were considered:



The intermediates I–IV described in the above equations were modeled and optimized with the same computational parameters as those of the reactant (3-NA). The energy of the other chemical species involved in the reactions ($NaBH_4$, H_2O , H_3BO_3 , $NaOH$ and H_2) was also calculated. The energies of the reactant, different intermediates and final diamine product (1,3-phenylenediamine) relative to that of the isolated 3-NA molecule that result from the above reaction steps are shown in Fig. 8a, both in the presence (red lines) and absence (blue lines) of $MoSe_2$. In this plot, the energy difference between both cases represents the adsorption energy of the different chemical species on the TMD surface. It should be noted that Fig. 8a depicts energy differences between hypothetical stable intermediates and not energy barriers associated to transition states. Likewise, although Bae et al. included a fifth intermediate in their calculations, which derived from attack of the hydroxylamino group in intermediate IV by a hydride, in our case such a fifth intermediate was not stable (neither the isolated molecule nor the $MoSe_2$ -molecule complex). This could be rationalized in terms of its Lewis structure, where an octet for the nitrogen was not achievable.

In the first step of the reaction, a hydride attacked the nitrogen atom of 3-NA to give intermediate I, the negative charge of which was balanced by a nearby sodium cation. In the presence of $MoSe_2$, the two oxygen atoms retained their bonding to the unsaturated molybdenum atoms from a selenium vacancy, with little changes in the corresponding bond distances. However, for intermediate II (3-nitrosoaniline) there was a substantially increased bonding of the molecule to the TMD surface via the nitroso group, with oxygen-molybdenum and nitrogen-molybdenum distances of 2.16 and 2.12 Å, respectively. As a result, the adsorption energy for this intermediate was the greatest. Here, the selenium vacancy in $MoSe_2$ allowed for a deep vertical penetration of the nitroso group. In the third step, a second hydride attacked the nitroso group to give intermediate III, which led to a large overall stabilization of the system, both in the presence and absence of $MoSe_2$, and was associated to a significant adsorption energy with the TMD that mainly stemmed from interaction with the sodium cation. It is worth noting that the oxygen-molybdenum and nitrogen-molybdenum interactions disappeared in this intermediate, and it was the hydrogen atom from the NHO^{\ominus} group that was pointing to the vacancy. In the fourth step, the oxygen from the NHO^{\ominus} group captured a hydrogen from a nearby water molecule, yielding 3-hydroxylaminoaniline (intermediate IV). In this case, the stabilization of the system as a result of interaction with $MoSe_2$ was the lowest among all the intermediates, so that the corresponding adsorption energy was comparable to that of the reactant and final product. Again, interaction of unsaturated molybdenum atoms with the oxygen and nitrogen from the hydroxylamino group was stymied by its hydrogen atoms. Lastly, a third hydride attacked the hydroxylamino

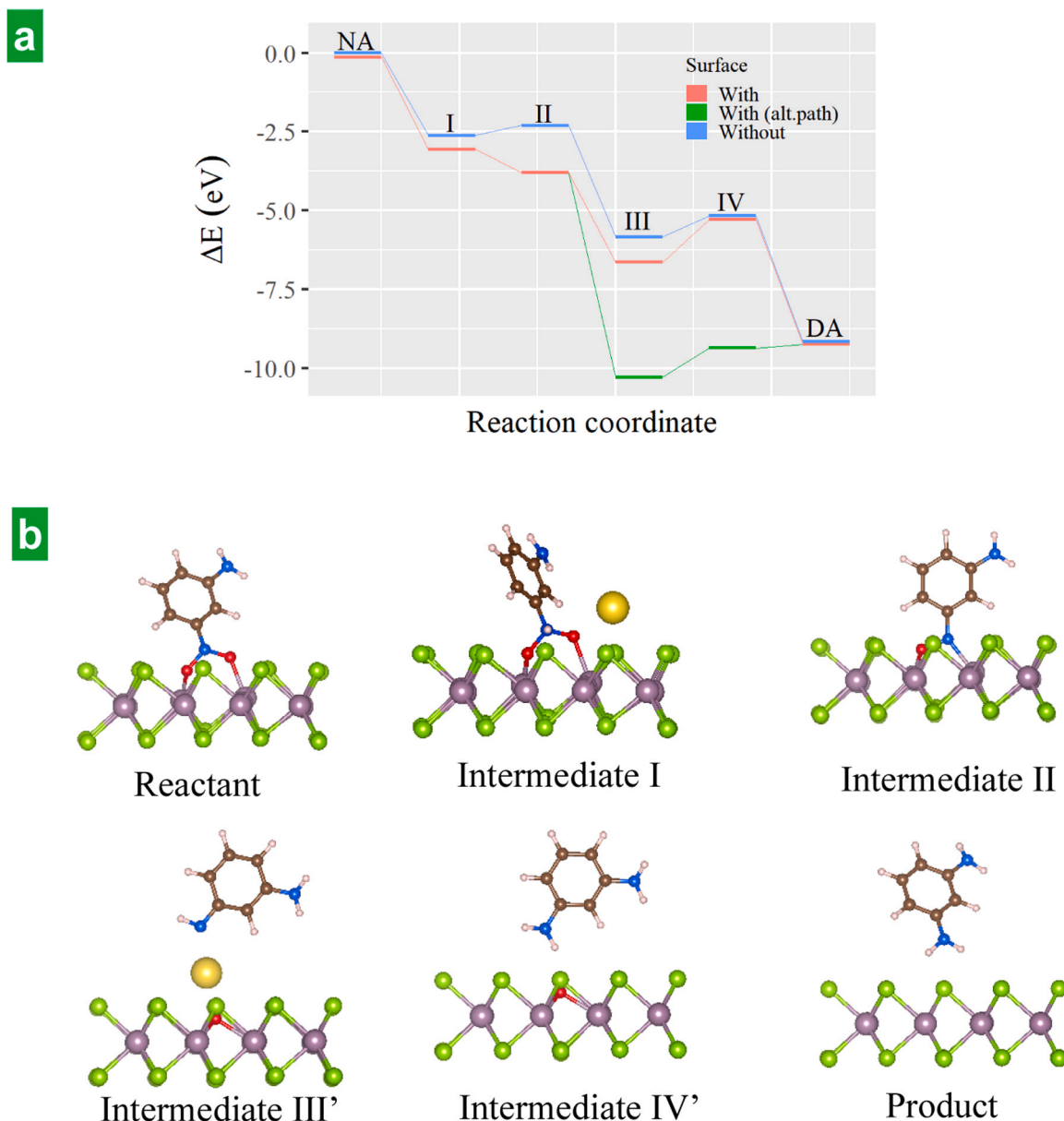
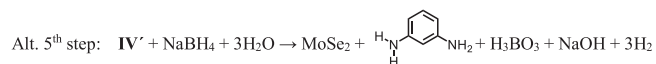
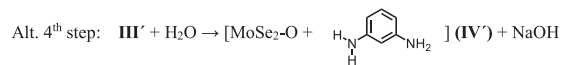
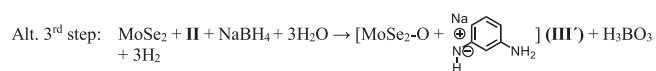


Fig. 8. Energetics of the reaction in the absence and in the presence of MoSe₂ catalyst by different reaction mechanisms, including one originally proposed here. (a) Calculated energies of the reaction intermediates and the reaction product relative to that of isolated 3-NA in the presence (red lines) and absence (blue lines) of MoSe₂ along a mechanism similar to that proposed by Bae et al. for 4-NP reduction by NaBH₄ with magnetite (111) surface as the catalyst [85]. Energies associated to the alternative reaction pathway suggested in this work (green lines). (b) Equilibrium geometries for the initial reactant, different intermediates and final diamine product along the latter reaction pathway.

group, yielding the final diamine product (fifth step). The feasibility of the proposed mechanism was experimentally supported by the detection of some of the reaction intermediates, namely, 3-nitrosoaniline (intermediate II) and 3-hydroxylaminoaniline (intermediate IV), by means of UHPLC/HR-MS (see section S9 in the SM).

Nonetheless, while the former can be considered the classical reaction pathway for reduction of the nitro group, we noticed that an energetically competitive, alternative pathway was possible on the MoSe₂ surface. Specifically, when the oxygen atom from intermediate III was pointing to the selenium vacancy of the TMD, the molecule dissociated spontaneously, resulting in the vacancy being passivated by the oxygen atom. This suggested an alternative pathway for the third, fourth and fifth steps of the reaction, which could take place as follows:



Here, MoSe₂-O denotes the TMD surface with a selenium vacancy filled by an oxygen atom. The energies associated to this alternative reaction pathway are given in Fig. 8a (green lines) and the corresponding equilibrium geometries for initial reactant, different

intermediates and final diamine product are presented in Fig. 8b. In this third step, the N-O bond was broken upon hydride attack, leading to passivation of a selenium vacancy in MoSe₂ by the oxygen atom. In the resulting intermediate (III), the sodium ion was located between the TMD surface and the negatively charged arene molecule. In the fourth step, reaction of intermediate III with a water molecule yielded the final diamine product adsorbed on the passivated vacancy (intermediate IV). Here, a hydrogen atom from the newly generated amino group was pointing to the vacancy-adsorbed oxygen in a plausible hydrogen bonding interaction (H-O distance of 2.18 Å). In the fifth step a hydride attacked the oxygen passivating the vacancy, which allowed regeneration of the latter. Finally, the target diamine product could readily desorb from the original, regenerated MoSe₂ surface. As the intermediates III and IV implied in this alternative mechanism are not isolable in solution, they could not be possibly detected by UHPLC/HR-MS. Their detection would probably require the use of a very sensitive, in situ characterization technique applicable to specimens in solid state, maybe even implying synchrotron radiation, which is out of the scope of this work. However, we note that the lack of experimental evidence of its intermediates does not preclude the actual occurrence of this or other energetically feasible pathways.

3.5. Colloidal stabilization and immobilization of the MoSe₂ nanosheet catalyst

While working with bare MoSe₂ flakes dispersed in water was useful to reveal their intrinsic catalytic activity, we note that the practical utility of the catalyst for water treatment under such conditions was limited due to the strictly time-bound colloidal stability of the bare flakes. To address this issue, the latter could be stabilized by means of proper dispersing agents (e.g., small molecules or polymers), but the adsorption of such chemical species on the surface of the nanosheets was likely to impact their catalytic performance, which therefore needed to

be elucidated. Here, the bare exfoliated MoSe₂ flakes were stabilized with the aid of either a small molecule, namely, the nucleotide adenosine monophosphate (AMP), or a triblock polymer, i.e., Pluronic P123 [(poly(ethylene glycol)-*block*-poly(propylene glycol)-*block*-poly(ethylene glycol))]. Both compounds have been previously shown to be highly efficient as colloidal dispersants for TMD nanosheets [86,87]. Fig. 9a compares the reaction kinetic profiles obtained with the bare MoSe₂ flakes (black traces) with those recorded with the AMP- and P123-stabilized flakes (red and blue traces, respectively) for the reduction of 3-NA. As could be expected, slower reduction rates were seen for the catalyst stabilized with the (macro)molecular compounds. This was most likely the result of competitive adsorption of the reagent and the dispersant at the catalytic active sites of MoSe₂ [65]. However, we note that the decrease in catalytic activity of the colloiddally stabilized nanosheets was not very drastic, which was positive with a view to their practical implementation. In contrast, the activity of the exfoliated MoS₂ nanosheets was seen to decrease to a larger degree after their colloidal stabilization by the same means (data not shown), resulting in much longer reduction times (as well as much longer induction periods). This highlighted once again the superiority of the 2D MoSe₂ catalyst over its MoS₂ counterpart.

As an alternative to the use of colloidal dispersants, the bare MoSe₂ nanosheets could also be immobilized on a suitable polymeric scaffold, which facilitated the manipulation and re-use of the catalyst. For example, the nanosheets were supported onto melamine foam by a straightforward dip-coating process. Whereas the starting foam exhibited a white color together with a smooth and essentially featureless surface [see digital photograph (inset) and field emission scanning electron microscopy (FE-SEM) image in Fig. 9b], its MoSe₂-coated counterpart became gray-green and developed a rough surface (Fig. 9c). Closer inspection of the coated foam (Fig. 9d) revealed a film of MoSe₂ flakes covering the polymeric substrate. The melamine foam-supported flakes were able to catalyze the reduction of, e.g., 3-NA, as noticed from

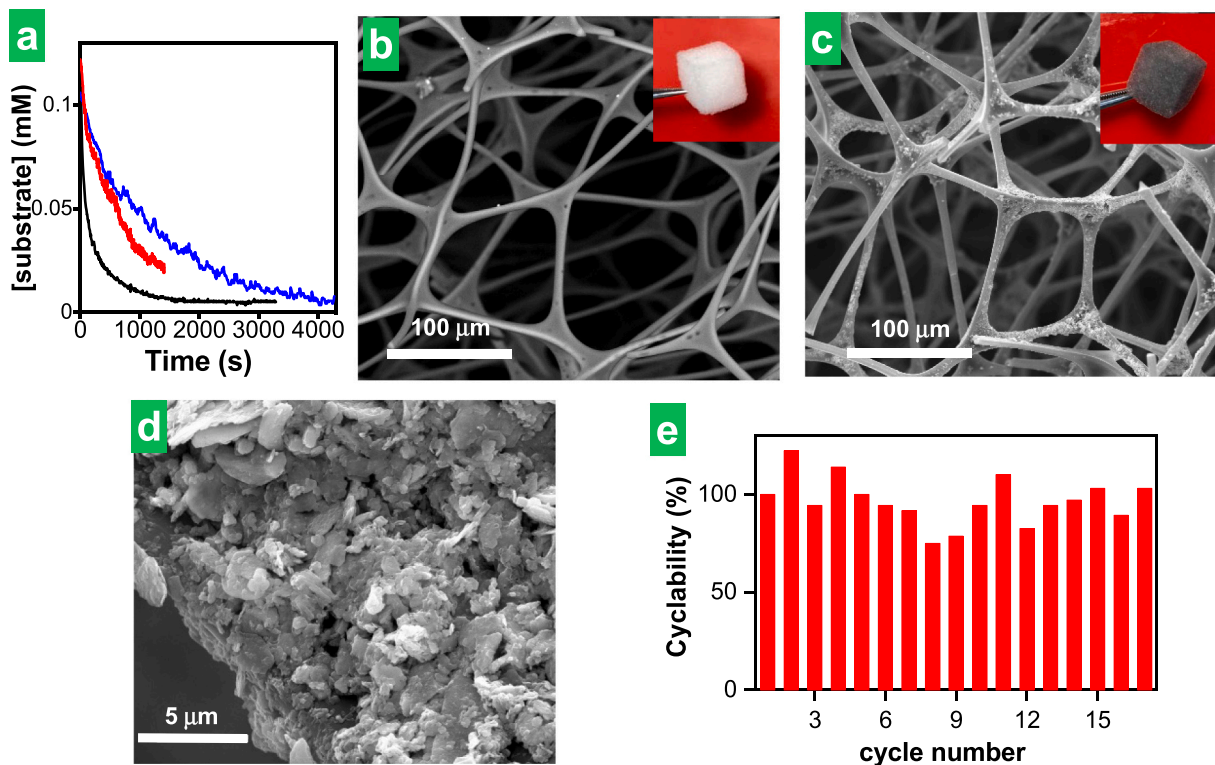


Fig. 9. Colloidal stabilization and immobilization of the MoSe₂ catalyst (a) Kinetic profiles obtained with the bare MoSe₂ flakes (black traces) and with AMP- and P123-stabilized flakes (red and blue traces, respectively) for the reduction of 3-NA. FE-SEM images of (b) bare melamine foam and (c,d) MoSe₂-coated foam. Inset to c and d: digital photographs of the corresponding foams. (e) Reusability experiments of melamine foam-supported MoSe₂ flakes in the catalytic reduction of 3-NA with NaBH₄ ([3-NA] = 0.11 mM).

the discoloration of the reaction medium and the emergence of the signature absorption spectrum of the reaction product. Further, they could be re-used for at least 15 consecutive reaction cycles without experiencing a substantial decline in activity (Fig. 9e), even if the foam was removed from the reaction medium, rinsed with water and finally squeezed to expel the water after each cycle. Additional information on the cycling of the catalyst is provided in section S10 of the SM. Specifically, the reaction conversion efficiency was evaluated for ten consecutive cycles and found to be consistent with ~100% reaction conversion efficiency (Fig. S14a and accompanying text). Moreover, characterization of the used catalyst by Raman and XPS spectroscopy (Figs. S14b-d of the SM) confirmed that its structural and chemical features were preserved throughout the cycling process. Indeed, the Raman and XPS spectra of the cycled catalyst are very similar or even coincident within experimental error with those of the freshly prepared catalyst.

Apart from establishing the practical utility of the MoSe₂ catalyst in the context of water remediation, the feasibility of its use as catalyst for synthetic applications was also confirmed by performing tests using a higher substrate concentration (1 mM) compatible with synthetic applications for some selected nitroarenes. 4-NP was chosen because its reduction is essential in the pharmaceutical industry for the manufacture of analgesics and antipyretics, such as paracetamol [88], and other drugs, as well as for the manufacture of photographic developers, corrosion inhibitors, and anticorrosion lubricants [69]. 4-NA has also industrial relevance as a precursor to p-phenylenediamine though catalyzed reduction, which is the starting material for the synthesis of dyes [89]. As the mechanistic study in this work focuses on 3-NA reduction, testing it for synthetic applications as well was deemed necessary to offer a comprehensive study. The tests confirmed the feasibility of the use of MoSe₂ as a catalyst for synthesis, given that the reduction of 4-NP, 4-NA, and 3-NA could be successfully carried out at a higher substrate concentration as well (see Fig. S15 in section S11 of the SM).

4. Conclusions

An investigation of two-dimensional (2D) MoSe₂ nanosheets as a catalyst for the reduction of nitroarenes into their corresponding anilines has revealed this transition metal dichalcogenide (TMD) to be more active than its MoS₂ counterpart. This indicated that the traditional focus on the latter as the TMD catalyst of choice for such reactions is not justified from the perspective of performance, opening the prospect for a broader exploration of the family of TMD compounds toward water remediation. The experimental results indicated that nitroarene reduction was faster on the MoSe₂ nanosheets by a factor of about 1.5–4.5 compared to their MoS₂ counterpart. The reaction kinetic profiles recorded with different nitroarenes were also qualitatively different for the two TMDs, implying the occurrence of diverging reaction orders, more specifically, first order for MoSe₂ and zero-order for MoS₂ relative to the substrate molecule. A comparative analysis of the factors that can influence the kinetic behaviors observed for different TMD catalysts suggested that conversion of nitroarene molecules adsorbed at the active sites was much faster on MoSe₂ than it was on MoS₂. In line with recent understanding of the catalytic activity of molybdenum-based materials toward the hydrogen evolution reaction, such an outcome was interpreted to originate from the lower electronegativity of selenium relative to sulfur. This distinct electronegativity led to a higher reducibility of the catalytic active sites (unsaturated molybdenum centers) and thus to a higher availability of active reducing species (hydrides) on the active sites of MoSe₂ compared to MoS₂. Density functional theory studies yielded insight into the origin of the different catalytic activities that the MoSe₂ nanosheets exhibited toward different nitroarene isomers (e.g., 3-nitroaniline > 4-nitroaniline > 2-nitroaniline) and suggested a novel pathway for the catalyzed reduction of the nitro group that involved oxygen passivation and subsequent regeneration of the active sites of MoSe₂. Finally, we believe the present work provides a rational basis for

the exploration and identification of TMDs beyond MoS₂ as enhanced catalysts for the reduction of nitroarenes and other organic compounds.

CRedit authorship contribution statement

Alberto Martínez-Jódar: Investigation, Validation, Formal analysis, Methodology, Data curation, Writing – review & editing. **Silvia Villar-Rodil:** Conceptualization, Investigation, Validation, Formal analysis, Methodology, Data curation, Visualization, Supervision, Project administration; Writing – review & editing. **Miguel A. Salvadó:** Methodology, Investigation, Visualization, Writing – review & editing. **D. F. Carrasco:** Investigation, Validation, Formal analysis, Data curation; **Pilar Pertierra:** Methodology, Investigation, Visualization, Writing – review & editing. **José M. Recio:** Investigation, Writing – review & editing. **Juan I. Paredes:** Conceptualization, Methodology, Formal analysis, Supervision, Resources, Project administration, Funding acquisition, Writing – original draft, Writing – review & editing.

Declaration of Competing Interest

The authors declare that they have no known competing financial interests or personal relationships that could have appeared to influence the work reported in this paper.

Data Availability

Data will be made available on request.

Acknowledgements

A. M.-J., S. V.-R., D. F. C., J. I. P. gratefully acknowledge funding by the Spanish Ministerio de Ciencia e Innovación and Agencia Estatal de Investigación (MCIN/AEI/ 10.13039/501100011033) as well as the European Regional Development Fund (ERDF, A way of making Europe) through grant PID2021-125246OB-I00, and by Plan de Ciencia, Tecnología e Innovación (PCTI) 2018-2022 del Principado de Asturias and the ERDF through grant IDI/2021/000037. A. M.-J. is grateful to the Spanish MINECO for his pre-doctoral contract (PRE2019-087583). The characterization of the graphene dispersions by DLS was performed at the ICTS NANBIOSIS by the Nanostructured Liquids Unit (U12) of the CIBER in Bioengineering, Biomaterials & Nanomedicine (CIBER-BBN), located at the IQAC-CSIC. M. A. S., P. P. and J. M. R. gratefully acknowledge funding by the Spanish Ministerio de Ciencia e Innovación and Agencia Estatal de Investigación (MCIN/AEI/10.13039/501100011033) as well as the European Regional Development Fund (ERDF, A way of making Europe) through grant PID2021-122585NB-C21, and by the Principado de Asturias and the ERDF through grant AYUD/2021/51036. We are very grateful to Dr. Alaa Adawy from the Laboratory of High-Resolution Transmission Electron Microscopy and to Dr. Pablo Manrique García from the Mass Spectrometry Laboratory (Scientific and Technical Services, University of Oviedo) for their expert assistance with the HR-TEM and SAED measurements, and the UHPLC/HR-MS analyses, respectively.

Appendix A. Supporting information

Supplementary data associated with this article can be found in the online version at [doi:10.1016/j.apcatb.2023.123174](https://doi.org/10.1016/j.apcatb.2023.123174).

References

- [1] D. Deng, K.S. Novoselov, Q. Fu, N. Zheng, Z. Tian, X. Bao, Catalysis with two-dimensional materials and their heterostructures, *Nat. Nanotechnol.* 11 (2016) 218–230.
- [2] H. Jin, C. Guo, X. Liu, J. Liu, A. Vasileff, Y. Jiao, Y. Zheng, S.-Z. Qiao, Emerging two-dimensional nanomaterials for electrocatalysis, *Chem. Rev.* 118 (2018) 6337–6408.

- [3] J. Di, J. Xiong, H. Li, Z. Liu, Ultrathin 2D photocatalysts: electronic-structure tailoring, hybridization, and applications, *Adv. Mater.* 30 (2018), 1704548.
- [4] A. Kumar, Q. Xu, Two-dimensional layered materials as catalyst supports, *ChemNanoMat* 4 (2018) 28–40.
- [5] L.X. Chen, Z.W. Chen, M. Jiang, Z. Lu, C. Gao, G. Cai, C.V. Singh, Insights on the dual role of two-dimensional materials as catalysts and supports for energy and environmental catalysis, *J. Mater. Chem. A* 9 (2021) 2018–2042.
- [6] H. Yin, Y. Dou, S. Chen, Z. Zhu, P. Liu, H. Zhao, 2D electrocatalysts for converting earth-abundant simple molecules into value-added commodity chemicals: recent progress and perspectives, *Adv. Mater.* 32 (2020), 1904870.
- [7] Q. Fu, X. Bao, Surface chemistry and catalysis confined under two-dimensional materials, *Chem. Soc. Rev.* 46 (2017) 1842–1874.
- [8] J. Deng, D. Deng, X. Bao, Robust catalysis on 2D materials encapsulating metals: concept, application, and perspective, *Adv. Mater.* 29 (2017), 1606967.
- [9] C. Zhu, D. Gao, J. Ding, D. Chao, J. Wang, TMD-based highly efficient electrocatalysts developed by combined computational and experimental approaches, *Chem. Soc. Rev.* 47 (2018) 4332–4356.
- [10] X. Wu, H. Zhang, J. Zhang, X.W. Lou, Recent advances on transition metal dichalcogenides for electrochemical energy conversion, *Adv. Mater.* 33 (2021), 2008376.
- [11] S. Jayabal, G. Saranya, J. Wu, Y. Liu, D. Geng, X. Meng, Understanding the high-electrocatalytic performance of two-dimensional MoS₂ nanosheets and their composite materials, *J. Mater. Chem. A* 5 (2017) 24540–24563.
- [12] Z. Li, N.H. Attanayake, J.L. Blackburn, E.M. Miller, Carbon dioxide and nitrogen reduction reactions using 2D transition metal dichalcogenide (TMD) and carbide/nitride (MXene) catalysts, *Energy Environ. Sci.* 14 (2021) 6242–6286.
- [13] L. Guardia, J.I. Paredes, J.M. Munuera, S. Villar-Rodil, M. Ayán-Varela, A. Martínez-Alonso, J.M.D. Tascón, Chemically exfoliated MoS₂ nanosheets as an efficient catalyst for reduction reactions in the aqueous phase, *ACS Appl. Mater. Interfaces* 6 (2014) 21702–21710.
- [14] M. Orlandi, D. Brenna, R. Harms, S. Jost, M. Benaglia, Recent developments in the reduction of aromatic and aliphatic nitro compounds to amines, *Org. Process Res. Dev.* 22 (2018) 430–445.
- [15] A.C. Poulse, G. Zoppellaro, I. Konidakis, E. Serpetzoglou, E. Stratakis, O. Tomanec, M. Beller, A. Bakandritsos, R. Zboril, Fast and selective reduction of nitroarenes under visible light with an earth-abundant plasmonic photocatalyst, *Nat. Nanotechnol.* 17 (2022) 485–492.
- [16] H. Hu, J.H. Xin, H. Hu, X. Wang, D. Miao, Y. Liu, Synthesis and stabilization of metal nanocatalysts for reduction reactions – a review, *J. Mater. Chem. A* 3 (2015) 11157–11182.
- [17] Z. Xiong, H. Zhang, W. Zhang, B. Lai, G. Yao, Removal of nitrophenols and their derivatives by chemical redox: a review, *Chem. Eng. J.* 359 (2019) 13–31.
- [18] K. Zhang, J.M. Suh, J.-W. Choi, H.W. Jang, M. Shokouhimehr, R.S. Varma, Recent advances in the nanocatalyst-assisted NaBH₄ reduction of nitroaromatics in water, *ACS Omega* 4 (2019) 483–495.
- [19] K. Peng, L. Fu, J. Ouyang, H. Yang, Emerging parallel dual 2D composites: natural clay mineral hybridizing MoS₂ and interfacial structure, *Adv. Funct. Mater.* 26 (2016) 2666–2675.
- [20] A.A. Jeffery, S.R. Rao, M. Rajamathi, Preparation of MoS₂-reduced graphene oxide (rGO) hybrid paper for catalytic applications by simple exfoliation-costacking, *Carbon* 112 (2017) 8–16.
- [21] K. Peng, L. Fu, H. Yang, J. Ouyang, A. Tang, Hierarchical MoS₂ intercalated clay hybrid nanosheets with enhanced catalytic activity, *Nano Res.* 10 (2017) 570–583.
- [22] N. Meng, J. Cheng, Y. Zhou, W. Nie, P. Chen, Green synthesis of layered 1T-MoS₂/reduced graphene oxide nanocomposite with excellent catalytic performances for 4-nitrophenol reduction, *Appl. Surf. Sci.* 396 (2017) 310–318.
- [23] Y. Li, Q. Chen, Z. Zhang, Q. Li, X. Qiao, Effects of morphology and crystallinity of MoS₂ nanocrystals on the catalytic reduction of *p*-nitrophenol, *J. Nanopart. Res.* 20 (2018), 327.
- [24] C. Nethravathi, A.D. Manganahalli, M. Rajamathi, Bi₂Te₃-MoS₂ layered nanoscale heterostructures for electron transfer catalysis, *ACS Appl. Nano Mater.* 2 (2019) 2005–2012.
- [25] S. García-Dalí, J.I. Paredes, B. Caridad, S. Villar-Rodil, M. Díaz-González, C. Fernández-Sánchez, A. Adawy, A. Martínez-Alonso, J.M.D. Tascón, Activation of two-dimensional MoS₂ nanosheets by wet-chemical sulfur vacancy engineering for the catalytic reduction of nitroarenes and organic dyes, *Appl. Mater. Today* 20 (2020), 100678.
- [26] S. García-Dalí, J.I. Paredes, S. Villar-Rodil, A. Martínez-Jódar, A. Martínez-Alonso, J.M.D. Tascón, Molecular functionalization of 2H-phase MoS₂ nanosheets via an electrolytic route for enhanced catalytic performance, *ACS Appl. Mater. Interfaces* 13 (2021) 33157–33171.
- [27] A. Ramalingam, E. Samaraj, S. Venkateshwaran, S.M. Senthilkumar, G.C. Senadi, 1T-MoS₂ catalysed reduction of nitroarenes and a one-pot synthesis of imines, *N. J. Chem.* 46 (2022) 8720–8728.
- [28] X. Pan, R.M. Sarhan, Z. Kochovski, G. Chen, A. Taubert, S. Mei, Y. Lu, Template synthesis of dual-functional porous MoS₂ nanoparticles with photothermal conversion and catalytic properties, *Nanoscale* 14 (2022) 6888–6901.
- [29] Y. Shi, W. Zhang, J. Tan, T. Yan, Y. Jia, Z. Wang, Y. Tang, Q. Gao, Intercalation-driven defect-engineering of MoS₂ for catalytic transfer hydrogenation, *Adv. Mater. Interfaces* 9 (2022), 2200505.
- [30] J. Tan, J. Shao, Y. Shi, W. Zhang, Q. Gao, Selective electrocatalytic hydrogenation of nitroarenes on interlayer-expanded MoS₂, *ACS Sustain. Chem. Eng.* 10 (2022) 13525–13533.
- [31] B. Chen, Q. Zhang, P. Zhao, M. Cen, Y. Song, W. Zhao, W. Peng, Y. Li, F. Zhang, X. Fan, Coupled Co-doped MoS₂ and CoS₂ as the dual-active site catalyst for chemoselective hydrogenation, *ACS Appl. Mater. Interfaces* 15 (2023) 1317–1325.
- [32] Y. Wen, H. Zhang, S. Zhang, One-step gas-solid reaction synthesis of W@WS₂ nanorattles and their novel catalytic activity, *Nanoscale* 6 (2014) 13090–13096.
- [33] Y. Sun, A.J. Darling, Y. Li, K. Fujisawa, C.F. Holder, H. Liu, M.J. Janik, M. Terrones, R.E. Schaak, Defect-mediated selective hydrogenation of nitroarenes on nanostructured WS₂, *Chem. Sci.* 10 (2019) 10310–10317.
- [34] M. Ling, B. Jiang, X. Cao, T. Wu, Y. Cheng, P. Zeng, L. Zhang, W.-C.M. Cheong, K. Wu, A. Huang, X. Wei, Phase-controllable synthesis of multifunctional 1T-MoS₂ nanostructures: applications in lithium-ion batteries, electrocatalytic hydrogen evolution, and the hydrogenation reaction, *ChemElectroChem* 8 (2021) 4148–4155.
- [35] A. Eftekhari, Molybdenum diselenide (MoSe₂) for energy storage, catalysis, and optoelectronics, *Appl. Mater. Today* 8 (2017) 1–17.
- [36] Y. Deng, S. Xiao, Y. Zheng, X. Rong, M. Bai, Y. Tang, T. Ma, C. Cheng, C. Zhao, Emerging electrocatalytic activities in transition metal selenides: synthesis, electronic modulation, and structure-performance correlations, *Chem. Eng. J.* 451 (2023), 138514.
- [37] H.-P. Komsa, J. Kotakoski, S. Kurasch, O. Lehtinen, U. Kaiser, A.V. Krashenninnikov, Two-dimensional transition metal dichalcogenides under electron irradiation: defect production and doping, *Phys. Rev. Lett.* 109 (2012), 035503.
- [38] V. Lykourinou, A.I. Hanafy, K.S. Bisht, A. Angerhofer, L.-J. Ming, Iron(III) Complexes of metal-binding copolymers as proficient catalysts for acid hydrolysis of phosphodiester and oxidative DNA cleavage – insight into the rational design of functional metallopolymers, *Eur. J. Inorg. Chem.* (2009) 1199–1207.
- [39] J.H. Scofield, Hartree-Slater subshell photoionization cross-sections at 1254 and 1487 eV, *J. Electro Spectrosc. Relat. Phenom.* 8 (1976), 129–137.
- [40] G. Kresse, J. Furthmüller, Efficiency of ab-initio total energy calculations for metals and semiconductors using a plane-wave basis set, *Comput. Mater. Sci.* 6 (1996) 15–50.
- [41] G. Kresse, D. Joubert, From ultrasoft pseudopotentials to the projector augmented-wave method, *Phys. Rev. B* 59 (1999) 1758–1775.
- [42] J.P. Perdew, K. Burke, M. Ernzerhof, Generalized gradient approximation made simple, *Phys. Rev. Lett.* 77 (1996) 3865–3868.
- [43] W. Kraus, G. Nolze, POWDER CELL - a program for the representation and manipulation of crystal structures and calculation of the resulting X-ray powder patterns, *J. Appl. Cryst.* 29 (1996) 301–303.
- [44] K. Momma, F. Izumi, VESTA: a three-dimensional visualization system for electronic and structural analysis, *J. Appl. Crystallogr.* 41 (2008) 653–665.
- [45] G. Cunningham, M. Lotya, C.S. Cucinotta, S. Sanvito, S.D. Bergin, R. Menzel, M.S. P. Shaffer, J.N. Coleman, Solvent exfoliation of transition metal dichalcogenides: dispersibility of exfoliated nanosheets varies only weakly between compounds, *ACS Nano* 4 (2012) 3468–3480.
- [46] N. Dong, Y. Li, Y. Feng, S. Zhang, X. Zhang, C. Chang, J. Fan, L. Zhang, J. Wang, Optical limiting and theoretical modeling of layered transition metal dichalcogenide nanosheets, *Sci. Rep.* 5 (2015), 14646.
- [47] Y.-H. Chang, W. Zhang, Y. Zhu, Y. Han, J. Pu, J.-K. Chang, W.-T. Hsu, J.-K. Huang, C.-L. Hsu, M.-H. Chiu, T. Takenobu, H. Li, C. Wu, W.-H. Chang, A.T.S. Wee, L.-J. Li, Monolayer MoSe₂ grown by chemical vapor deposition for fast photodetection, *ACS Nano* 8 (2014) 8582–8590.
- [48] N. Lundt, A. Maryński, E. Cherotchenko, A. Pant, X. Fan, S. Tongay, G. Şek, A. V. Kavokin, S. Höfling, C. Schneider, Monolayered MoSe₂: a candidate for room temperature polaritonics, *2D Mater.* 4 (2017), 015006.
- [49] B.J. Berne, R. Pecora, *Dynamic light scattering, with applications to chemistry, biology and physics*, Dover Publications, Inc., New York, 2000, chapter 8.
- [50] M. Lotya, A. Rakovich, J.F. Donegan, J.N. Coleman, Measuring the lateral size of liquid-exfoliated nanosheets with dynamic light scattering, *Nanotechnology* 24 (2013), 265703.
- [51] D. Nam, J.-U. Lee, H. Cheong, Excitation energy dependent Raman spectrum of MoSe₂, *Sci. Rep.* 5 (2015), 17113.
- [52] P. Tonndorf, R. Schmidt, P. Böttger, X. Zhang, J. Börner, A. Liebig, M. Albrecht, C. Kloc, O. Gordan, D.R.T. Zahn, S.M. Vasconcellos, R. Bratschkitsch, Photoluminescence emission and Raman response of monolayer MoS₂, MoSe₂, and WSe₂, *Opt. Express* 21 (2013) 4908–4916.
- [53] X. Lu, M.L.B. Utama, J. Lin, X. Luo, Y. Zhao, J. Zhang, S.T. Pantelides, W. Zhou, S. Y. Quek, Q. Xiong, Rapid and nondestructive identification of polytypism and stacking sequences in few-layer molybdenum diselenide by Raman spectroscopy, *Adv. Mater.* 27 (2015) 4502–4508.
- [54] X. Lu, X. Luo, J. Zhang, S.Y. Quek, Q. Xiong, Lattice vibrations and Raman scattering in two-dimensional layered materials beyond graphene, *Nano Res* 9 (2016) 3559–3597.
- [55] G. Greczynski, L. Hultman, Impact of sample storage type on adventitious carbon and native oxide growth: X-ray photoelectron spectroscopy study, *Vacuum* 205 (2022), 111463.
- [56] A. Azcatl, K.C. Santos, X. Peng, N. Lu, S. McDonnell, X. Qin, F. de Dios, R. Addou, J. Kim, M.J. Kim, K. Cho, R.M. Wallace, HfO₂ on UV-O₃ exposed transition metal dichalcogenides: interfacial reactions study, *2D Mater.* 2 (2015), 014004.
- [57] M. Wu, N. Li, S. Zuo, W. Shen, G. Sun, Q. Li, M. Shi, J. Ma, Efficient charge separation via MoSe₂ nanosheets with tunable 1T phase contents: piezoreduction of Cr(VI) to Cr(III) and piezodegradation of RhB, *Inorg. Chem.* 61 (2022) 17972–17984.
- [58] L.-F. Huang, Z. Zeng, Roles of mass, structure, and bond strength in the phonon properties and lattice anharmonicity of single-layer Mo and W dichalcogenides, *J. Phys. Chem. C* 119 (2015) 18779–18789.
- [59] J.I. Paredes, J.M. Munuera, S. Villar-Rodil, L. Guardia, M. Ayán-Varela, A. Pagán, S.D. Aznar-Cervantes, J.L. Cenís, A. Martínez-Alonso, J.M.D. Tascón, Impact of covalent functionalization on the aqueous processability, catalytic activity, and

- biocompatibility of chemically exfoliated MoS₂ nanosheets, *ACS Appl. Mater. Interfaces* 8 (2016) 27974–27986.
- [60] R.J. Smith, P.J. King, M. Lotya, C. Wirtz, U. Khan, S. De, A. O'Neill, G.S. Duesberg, J.C. Grunlan, G. Moriarty, J. Chen, J. Wang, A.I. Minett, V. Nicolosi, J.N. Coleman, Large-scale exfoliation of inorganic layered compounds in aqueous surfactant solutions, *Adv. Mater.* 23 (2011) 3944–3948.
- [61] Z. Lei, W. Zhu, S. Xu, J. Ding, J. Wan, P. Wu, Hydrophilic MoSe₂ nanosheets as effective photothermal therapy agents and their application in smart devices, *ACS Appl. Mater. Interfaces* 8 (2016) 20900–20908.
- [62] M.R. Uhlig, D. Martin-Jimenez, R. Garcia, Atomic-scale mapping of hydrophobic layers on graphene and few-layer MoS₂ and WSe₂ in water, *Nat. Commun.* 10 (2019), 2606.
- [63] J. Kim, S. Kwon, D.-H. Cho, B. Kang, H. Kwon, Y. Kim, S.O. Park, G.Y. Jung, E. Shin, W.-G. Kim, H. Lee, G.H. Ryu, M. Choi, T.H. Kim, J. Oh, S. Park, S.K. Kwak, S.W. Yoon, D. Byun, Z. Lee, C. Lee, Direct exfoliation and dispersion of two-dimensional materials in pure water with temperature control, *Nat. Commun.* 6 (2015), 8294.
- [64] V. Forsberg, R. Zhang, J. Bäckström, C. Dahlström, B. Andres, M. Norgren, M. Andersson, M. Hummelgård, H. Olin, Exfoliated MoS₂ in water without additives, *PLoS One* 11 (2016), e0154522.
- [65] R.D. Neal, R.D. Hughes, P. Sapkota, S. Ptasińska, S. Neretina, Effect of nanoparticle ligands on 4-nitrophenol reduction: reaction rate, induction time, and ligand desorption, *ACS Catal.* 10 (2020) 10040–10050.
- [66] D.H. Everett, *Basic principles of colloid science*, Royal Society of Chemistry, London, 1988, chapters 3 and 8.
- [67] A. Jawaid, J. Che, L.F. Drummy, J. Bultman, A. Waite, M.-S. Hsiao, R.A. Vaia, Redox exfoliation of layered transition metal dichalcogenides, *ACS Nano* 11 (2017) 635–646.
- [68] A.M. Jawaid, A.J. Ritter, R.A. Vaia, Mechanism for redox exfoliation of layered transition metal dichalcogenides, *Chem. Mater.* 32 (2020) 6550–6565.
- [69] T. Aditya, A. Pal, T. Pal, Nitroarene reduction: a trusted model reaction to test nanoparticle catalysts, *Chem. Commun.* 51 (2015) 9410–9431.
- [70] E. Mennerov, R.A. Hughes, S. Neretina, Catalytic reduction of 4-nitrophenol: a quantitative assessment of the role of dissolved oxygen in determining the induction time, *Nano Lett.* 16 (2016) 7791–7797.
- [71] P. Hervés, M. Pérez-Lorenzo, L.M. Liz-Marzán, J. Dzubiella, Y. Lu, M. Ballauff, Catalysis by metallic nanoparticles in aqueous solution: model reactions, *Chem. Soc. Rev.* 41 (2012) 5577–5587.
- [72] J.A. Dean, *Langés Handbook of Chemistry*, 15th edition, McGraw-Hill, New York, section 8, pages 8.24–8.72.
- [73] J. Hong, Z. Hu, M. Probert, K. Li, D. Lv, X. Yang, L. Gu, N. Mao, Q. Feng, L. Xie, J. Zhang, D. Wu, Z. Zhang, C. Jin, W. Ji, X. Zhang, J. Yuan, Z. Zhang, Exploring atomic defects in molybdenum disulphide monolayers, *Nat. Commun.* 6 (2015) 6293.
- [74] D. Xiao, D.-L. Bao, X. Liang, Y. Wang, J. Shen, C. Cheng, P.K. Chu, Experimental and theoretical investigation of the control and balance of active sites on oxygen plasma-functionalized MoSe₂ nanosheets for efficient hydrogen evolution reaction, *Appl. Catal. B: Environ.* 288 (2021), 119983.
- [75] M. Wang, Z. Sun, H. Ci, Z. Shi, L. Shen, C. Wei, Y. Ding, X. Yang, J. Sun, Identifying the evolution of selenium-vacancy-modulated MoSe₂ precatalyst in lithium-sulfur chemistry, *Angew. Chem. Int. Ed.* 60 (2021) 24558–24565.
- [76] Y. Zhang, Y. Gao, S. Yao, S. Li, H. Asakura, K. Teramura, H. Wang, D. Ma, Sublimation-induced sulfur vacancies in MoS₂ catalyst for one-pot synthesis of secondary amines, *ACS Catal.* 9 (2019) 7967–7975.
- [77] F. Yang, C. Chi, C. Wang, Y. Wang, Y. Li, High graphite N content in nitrogen-doped graphene as an efficient metal-free catalyst for reduction of nitroarenes in water, *Green. Chem.* 18 (2016) 4254–4262.
- [78] Y. Cai, Z. Bai, H. Pan, Y.P. Feng, B.I. Yakobson, Y.-W. Zhang, Constructing metallic nanorods on a MoS₂ monolayer via hydrogenation, *Nanoscale* 6 (2014) 1691–1697.
- [79] J.A. Bau, R. Ahmad, L. Cavallo, M. Rueping, A unified theory for H₂ evolution on Mo-based electrocatalysts, *ACS Energy Lett.* 7 (2022) 3695–3702.
- [80] H. Tang, K. Dou, C.-C. Kaun, Q. Kuang, S. Yang, MoSe₂ nanosheets and their graphene hybrids: synthesis, characterization and hydrogen evolution reaction studies, *J. Mater. Chem. A* 2 (2014) 360–364.
- [81] J.D. Wiensch, J. John, J.M. Velazquez, D.A. Torelli, A.P. Pieterick, M.T. McDowell, K. Sun, X. Zhao, B.S. Brunshwig, N.S. Lewis, Comparative study in acidic and alkaline media of the effects of pH and crystallinity on the hydrogen-evolution reaction on MoS₂ and MoSe₂, *ACS Energy Lett.* 2 (2017) 2234–2238.
- [82] S. Wang, A. Robertson, J.H. Warner, Atomic structure of defects and dopants in 2D layered transition metal dichalcogenides, *Chem. Soc. Rev.* 47 (2018) 6764–6794.
- [83] Q. Liang, Q. Zhang, X. Zhao, M. Liu, A.T.S. Wee, Defect engineering of two-dimensional transition-metal dichalcogenides: applications, challenges, and opportunities, *ACS Nano* 15 (2021) 2165–2181.
- [84] P.-Y. Wang, B.-A. Chen, Y.-C. Lee, C.-C. Chiu, First-principles modeling of the highly dynamical surface structure of a MoS₂ catalyst with S-vacancies, *Phys. Chem. Chem. Phys.* 24 (2022) 24166–24172.
- [85] S. Bae, S. Gim, H. Kim, K. Hanna, Effect of NaBH₄ on properties of nanoscale zero-valent iron and its catalytic activity for reduction of *p*-nitrophenol, *Appl. Catal. B: Environ.* 182 (2016) 541–549.
- [86] N.D. Mansukhani, L.M. Guiney, P.J. Kim, Y. Zhao, D. Alducin, A. Ponce, E. Larios, M.J. Yacamán, M.C. Hersam, High-concentration aqueous dispersions of nanoscale 2D materials using nonionic, biocompatible block copolymers, *Small* 12 (2016) 294–300.
- [87] M. Ayán-Varela, O. Pérez-Vidal, J.I. Paredes, J.M. Munuera, S. Villar-Rodil, M. Díaz-González, C. Fernández-Sánchez, V.S. Silva, M. Cicuéndez, M. Vila, A. Martínez-Alonso, J.M.D. Tascón, Aqueous exfoliation of transition metal dichalcogenides assisted by DNA/RNA nucleotides: catalytically active and biocompatible nanosheets stabilized by acid-base interactions, *ACS Appl. Mater. Interfaces* 9 (2017) 2835–2845.
- [88] Ellis, Frank (2002). Paracetamol: a curriculum resource. Cambridge: Royal Society of Chemistry. ISBN 0–85404–375–6.
- [89] Gerald Booth, Aromatic Nitro Compounds Ullmann's Encyclopedia of Industrial Chemistry, Wiley-VCH, Weinheim, 2007.